PHOTOCURRENT GENERATION IN LOW DIMENSIONAL NANOMATERIALS

A THESIS SUBMITTED TO

THE GRADUATE SCHOOL OF ENGINEERING AND SCIENCE

OF BILKENT UNIVERSITY

IN PARTIAL FULFILLMENT OF THE REQUIREMENTS FOR

THE DEGREE OF

MASTER OF SCIENCE

IN

MATERIALS SCIENCE AND NANOTECHNOLOGY

By
Mohammadali Razeghi
November 2022

PHOTOCURRENT GENERATION IN LOW DIMENSIONAL NANOMATERIALS

By Mohammadali Razeghi

November 2022

We certify that we have read this thesis and that in our opinion it is fully adequate, in scope and in quality, as a thesis for the degree of Master of Science.

—

Talip Serkan Kasırga(Advisor)

Mehmet Cengiz Onbaşlı

Ibrahim Sarpkaya

Approved for the Graduate School of Engineering and Science:

Orhan Arıkan
Director of the Graduate School

ABSTRACT

PHOTOCURRENT GENERATION IN LOW DIMENSIONAL NANOMATERIALS

Mohammadali Razeghi
M.S. in Materials Science and Nanotechnology
Advisor: Talip Serkan Kasırga
November 2022

This thesis focuses on crucial issue on the understanding the underlying mechanisms of photoresponse in low-dimensional nanomaterials. As the size goes down to the micro and nano level, fine features and induced inhomogeneities like strain, thickness variation, substrate, and junctions become influential in determining plausible effects that can explain and control the light-matter interactions in an optoelectronic device. To develop a better understanding of the fundamental physical characteristics of nanomaterials and optimize thermal and electrical transport in nanomaterial devices, microscopic investigation at a single crystal level is required. In this thesis, I investigated photocurrent generation in two extreme cases: metallic silver nanowire (Ag NW) and semiconducting multilayer molybdenum disulfide (MoS2) using scanning photocurrent microscopy (SPCM). SPCM provides spatial mapping of photoresponse along with corresponding reflected light intensity with a few hundred nanometer resolution.

Two terminal devices of Ag and Ag network devices are made by drop-casting NW and placing indium as metal contacts. The SPCM maps show that the NW-NW junctions and NW-contacts interface locally enhance the plasmonic field and act as hot spots. The increased temperature at hot spots is enough to modulate the resistance and results in a photo-bolometric response under the bias voltage. To further enhance the photo-bolometric effect, we decorated the nanowires with plasmonic Ag nanoparticles. The nanoparticles increase the number of hot spots and strengthen light coupling into plasmons. We also attributed zero bias response to the photothermoelectric effect. The photocurrent is generated by the Seebeck coefficient difference caused by nanogaps and nonuniformities in the geometry along the Ag NW.

The second part of this thesis describes photocurrent generation by substrate engineering of a few-layer MoS2. To partially suspend a crystal, a flake of MoS2 is exfoliated and then transferred on a substrate with rectangular or circular holes. We observed photocurrent generation from the junction of the supported and suspended parts. Substrate effects like induced doping play an essential role in determining the properties of two-dimensional materials. Our investigations show that the Seebeck coefficient of the suspended part is changed due to isolation from the substrate. The difference in the Seebeck coefficient of suspended and supported regions forms a thermoelectric junction. We also investigated the impact of carrier type and concentration on photocurrent generation by gating experiments.

ÖZET

DÜŞÜK BOYUTLU MALZEMELERDE FOTOAKIM ÜRETIMI

Mohammadali Razeghi
Malzeme Bilimi ve Nanoteknoloji , Yüksek Lisans
Tez Danışmanı: Talip Serkan Kasırga
Kasım 2022

Bu tez, düşük boyutlu nanomalzemelerde foto tepki mekanizmalarının altında yatan çok önemli bir konuyu anlamaya odaklanmaktadır. Malzeme boyutu mikro ve nano seviyeye düştükçe, yapısal detaylar ve stres, kalınlık değişimi, alt taş ve eklemler gibi dış etmenlere bağlı düzensizlikler bir optoelektronik cihazdaki ışık-madde etkileşimlerini açıklayabilen ve kontrol edebilen olası etkilerin belirlenmesinde etkili olur. Nanomalzemelerin temel fiziksel özelliklerinin daha iyi anlaşılmasını sağlamak ve nanomalzeme aygıtlarda termal ve elektriksel taşımayı optimize etmek için tek bir kristal seviyesinde mikroskobik inceleme gereklidir.

Bu tezde, taramalı foto akım mikroskobu (SPCM) kullanarak iki olağanüstü durumda fotoakım üretimini araştırdım: metalik gümüş nanotel (Ag NW) ve yarı iletken çok katmanlı molibden disülfit (MoS_2). SPCM birkaç yüz nanometre çözünürlüğe karşılık gelen yansıyan ışık yoğunluğu ile birlikte foto tepkinin uzaysal haritalanmasını sağlar. İki uçlu Ag ve Ag nanotel ağ aygıtları nanotellerin damlatma biriktirilmesi ve metal kontak olarak indiyumun yerleştirilmesi ile yapıldı. SPCM haritaları, nanotel- nanotel bağlantılarının ve nanotel-kontak arayüzünün yerel olarak plazmonik alanı geliştirdiğini ve sıcak noktalar (hot-spots) olarak davrandığını göstermektedir. Sıcak noktalarda (hot-spots) artan sıcaklık, direncin değişimi için yeterlidir ve ön gerilim altında bir fotobolometrik tepki ile sonuçlanır. Fotobolometrik etkiyi daha da arttırmak için nanotelleri plazmonik Ag nano parçacıklarla donattık. Nano parçacıklar sıcak notların (hot-spots) sayısını ve plazmona bağlanan ışığı güçlendirirler. Aynı zamanda sıfır ön gerilim tepkisini fototermal etkiye dayandırdık. Fotoakım, Ag nanotel boyunca geometrideki nano boşluklar ve düzensizliklerin neden olduğu Seebeck katsayı farkı tarafından üretilmektedir.

Bu tezin ikinci kısmı, birkaç katmanlı MoS_2'nin alttaş mühendisliği (substrate engineering) ile foto akım üretimini açıklamaktadır Bir kristali kısmen askıya almak için, MoS_2 ince katmanlar ayrıştırıldı ve sonra üzerinde dikdörtgen veya dairesel delikleri bulunan alt taş üzerine aktarıldı.

Desteklenen ve askıda kalan parçaların birleşiminden fotoakım oluşumunu gözlemledik. İndüklenmiş katkılama (induced doping) gibi alt taş etk-ileri, iki boyutlu malzemelerin özelliklerinin belirlenmesinde önemli bir rol oynar. Araştırmalarımız, askıdaki parçanın alt taştan ayrılması nedeniyle Seebeck kat-sayısının değiştiğini göstermektedir. Askıya alınan ve desteklenen bölgelerin See-beck katsayısındaki fark, bir termoelektrik bağlantı oluşturur. Ayrıca kapı (gate) deneyleri ile taşıyıcı tipi ve yoğunluğunun fotoakım üretimi üzerindeki etkisini de araştırdık.

Anahtar sözcükler: Taramalı Fotoakım Mikroskobu, Gümüş Nanotel, Nanotel Ağı, Plazmon, Bolometrik Etki, Molibden Disülfür, Foto tepki, Foto Termoelek-trik Etki, Seebeck Katsayısı, Raman Spektroskopisi, 2B malzemele.

Acknowledgement

First and foremost, I am highly grateful to be lucky enough to work under the supervision of Dr. Talip Serkan Kasırga. His patience, support, and professionalism have paved my way through the scientific world, and her vision and ideas have been precious and constructive. I am sincerely thankful to him for giving me a free hand in my research, guiding me, and believing in me. I warmly appreciate my dissertation committee members, Dr. Mehmet Cengiz Onbasli and Dr. Ibrahim Sarpkaya for generously offering their time and support through reviewing this document.

I would like to thank Dr. Hilmi Volkan Demir, Merve Üstünçelik and Farzan Shabani for their contribution and valuable comments on the silver nanowire project. I am greatly thankful to my collaborators for lending me their expertise, Dr. Pascal Gehring and his research group at UCLouvain, who provided experimental support on substrate engineering of MoS_2.

I also would like to acknowledge current and previous members of SCM Lab members for their help in the lab work, especially Dr. Aji Abdulsalam Suleiman, Merve Üstünçelik, Amir Parsi, Uğur Başçı, Oğuzhan Oğuz, Doruk Pehlivanoğlu, Ali Sheraz and Engin Can Sürmeli.

It is hard to imagine finishing this journey without my family's support and endless care. I feel so grateful to have supportive and loving friends during these years Farzan, Pedram, Amir, Merve, Ata, Umut, Samet, Halit, Gunes, Olga, Mehdi, Mahnam, Melis, Eylul, Cansin, Rashid, Aydemir and Gun.

Contents

List of Figures

Chapter 1

Introduction to photocurrent

1.1   Photocurrent generation Mechanisms

Photocurrent generation in nanomaterials can be the result of simultaneous mechanisms. The amount and the mobility of charge carriers can modulate the conductivity of semiconducting materials. The photons reaching semiconducting materials can generate extra electrons and holes. In the photoconductive effect, the resistance of the material decreases as more charge carries generated by the light. By the illumination of photons above the band gap of semiconducting materials the excess carriers facilitate the current passing through the channels (Figure 1.1). Worth noting without applying external bias, there would not be a preferred direction of moving electrons and holes. As a consequence, this effect only manifested itself in the presence of bias voltage. In the photovoltaic effect, the generated electron and holes can be separated and produce a photocurrent by an internal electric field. The Schottky barrier at the semiconductor and metal interface or PN junction can form the built-in electric field needed to separate the

electrons and holes. Similar to the photoconductive effect, the incoming photons energy should be above the band gap to generate the electron and holes [1].
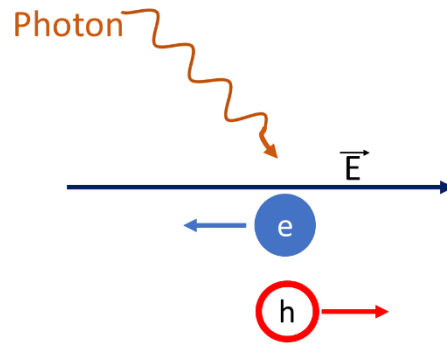
Figure 1.1 The schematic of the photovoltaic effect. If the energy of an incoming photon is more than the band gap energy of the semiconductor, it can excite electrons and holes. The electrons and holes are separated and generate photocurrent in the presence of the built-in electric field.

The thermal mechanisms can drive the carriers in the bolometric and photothermoelectric effects. These mechanisms are effective even with sub-band gap illumination. Change in material's resistance by heating cause a bolometric response. The bolometric effect can modulate the amount of current passing through the device by changing its resistance. The thermoelectric effect consists of heating the junction of two materials with different Seebeck coefficients. A light source can introduce the temperature gradient across the thermoelectric junction. This temperature gradient develops a photovoltage proportional to the difference in the Seebeck coefficient leading to photocurrent generation [1][2][3][4].
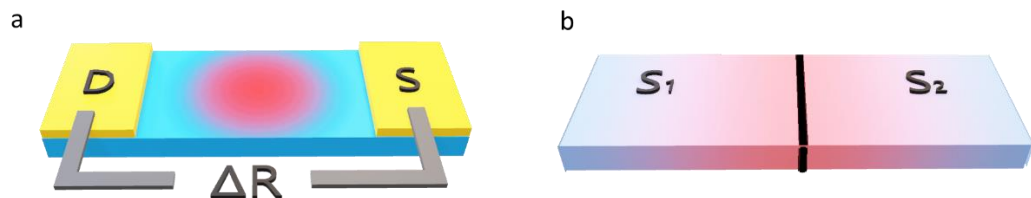
Figure 1.2: (a) Schematic of bolometric. Increasing the temperature causes a change in the resistance of the material. The resistance variation can be measured when a device is under bias voltage (b) Thermoelectric junction of two materials with

different Seebeck coefficients. Heating the junction develops the thermovoltage equals to $\Delta V = (S2 - S1) (T_{Hot} - T_{Cold})$,

1.2   Scanning Photocurrent Microscopy

The photoresponse of low dimensional materials is studied using scanning photocurrent microscopy (SPCM). A focused laser scans over the sample and photocurrent induced by the laser as a function of laser position is measured. The SPCM map is an image of photocurrents from each illuminated spot. The photodiode, located in the reflected light path, measures the intensity of the reflected light, which is then combined to plot the reflection map. So, we can relate a signal in the photocurrent map to the corresponding location in the reflection map.

Our setup has three different wavelengths 406, 532 and 633 nm lasers. Chopped laser light is focused on the sample using a 40x objective lens. The mechanical chopper controls the incident light frequency of the green laser (532 nm). The other two wavelengths are chopped electronically using the TTL output of the lock-in amplifier. Chopping the laser with a specific frequency enables the lock-in to amplify only the signals corresponding to the chopping frequency. The Lock-in amplifier then measures laser-induced change in current passing through the device using chopper frequency as an external reference. The photocurrent is obtained from two probes on the device. One contact of the device is grounded, and the other probe is attached to the pre-amplifier SR-570 to enhance the signal before feeding to the lock-in amplifier and can serve as a voltage bias source [5]. The schematic of the SPCM setup is shown in Figure 1.3.
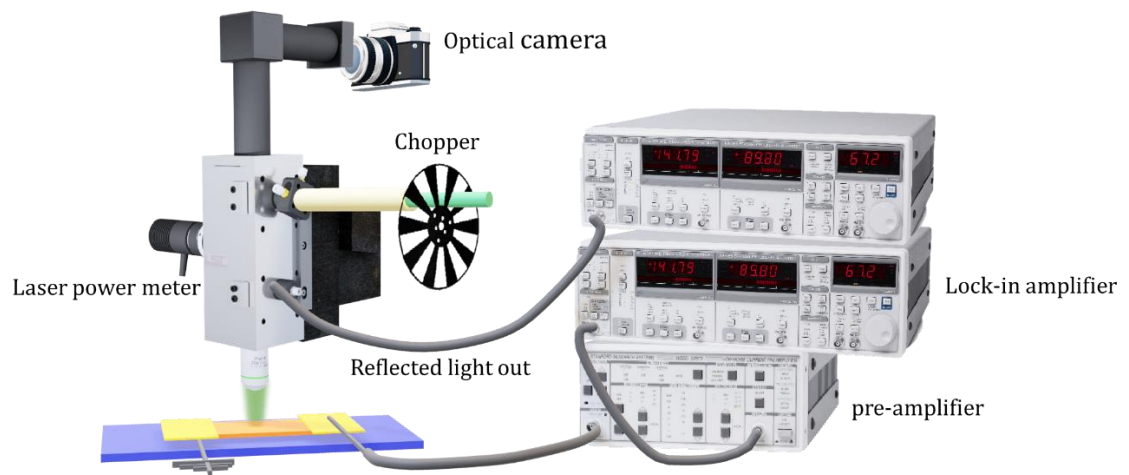
Figure 1.3 The schematic of the SPCM setup. The mechanical chopper modulates the frequency of the incident light. The signal from metallic probes amplified in the current pre-amplifier before being fed into lock-in amplifier.

Chapter 2

Plasmon-enhanced photoresponse of single silver nanowires and their network devices

2.1 Single Nanowire photoresponse

Despite the challenge of low stability of single silver nanowire (Ag NW), studying single NW devices is informing due to relative response simplicity over network and junction devices. For the device under bias voltage, local heating by the laser locally increases the device's resistance, resulting in a change in current passing through the channel. Plasmonic heating can enhance bolometric response by creating excess heat. We observed the polarization dependency of the photoconductive signal, which is a strong indication of the contribution of the plasmons in the heating process. Next, the alternating sign of the generated photocurrent in open circuit condition is attributed to the morphology changes along the nanowire, causing Seebeck modulation.

The photocurrent I_{PC} is the difference in current passing through the device with and without laser illumination. Lock-in amplifier measures I_{PC} as the resistance changes by laser illumination heating. In order to describe the bolometric response, we can take a derivative from Ohm's law [6][3]. The small change in resistance (δR) results in small change in current (I_{PC})

$$\delta R \approx -I_{PC}\frac{R_{2W}^2}{V}$$

The $\frac{I_{PC}}{V}$ can be expressed as negative photoconductance G_{PC}. The negative term implies that the conductance becomes less as the laser heat up the device.

$$\delta R \approx -G_{PC}R_{2W}^2$$

We can estimate the equivalent overall temperature increase of the device using the following equation

$$G_{Ph} \approx -\frac{1}{R^2}\frac{dR}{dT}\Delta T$$

The laser we are using is focused on a region less than a micrometer in size, and it cannot raise the temperature of the entire network uniformly. However, local heating can modulate the resistivity of the device. The propagating surface plasmons polaritons in the Ag NW device and subsequent plasmonic heating at the hot spot are the origins of the observed enhanced bolometric effect in the device.

Plasmons are the collective motion of free electrons on the interface of a metal and a dielectric. Metal nanostructures like NW and nanoparticles can support surface plasmons as they have free electrons. The light in free-space is transformed to the confined optical modes at the surface of a metal by the excitation of surface plasmons (Figure 2.1). The surface plasmons are divided into two classes based on confinement dimensions: localized surface plasmons and propagating surface plasmons, also called Surface Plasmon Polaritons (SPPs). Charge density waves, known as SPPs, are able to travel along the metal and dielectric interface up to tens of micrometers in distance and create a strong electromagnetic field in the near-field area surrounding the metal [6][7]. Because of the excitation of SPs, metal

6

NWs are of great interest due to their unique optical characteristics. The most common materials used in plasmonic NWs are gold and silver.
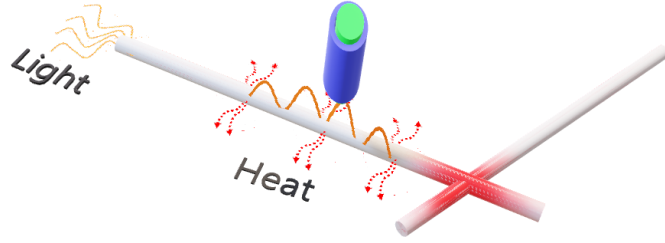
Figure 2.1 The incoming light can couple into plasmons in NW. The propagation of plasmons causes heating due to ohmic losses. The heating is more effective in the junction of NWs.

The optical image of the single NW device is shown in Figure 2.2a. The photocurrent (photoconductance) map of the device under 100mV bias voltage and the corresponding reflection map is shown in Figure 2.2b and c, respectively. We obtained photoconductance by dividing the photocurrent by the applied bias voltage ($\frac{I_{PC}}{V}$). As the bias voltage is constant during scanning, the photoconductance map is the same as the photocurrent map; only the color scale range is different. We observed negative photoconductance from almost the entire length of NW. The tilted and zoomed view of the scanning electron microscope (SEM) image depicts the flexibility of the NWs at nanoscale dimensions. The NW has bulged at the part located on top of a particle (Figure 2.2e), and the photoresponse is stronger close to the bulged area (marked by the orange box in Figure 2.2c). The momentum of incident laser light is less than the plasmons in the NW. Deflection in NW and scattering at symmetry breaking points provide the momentum difference required for coupling the incident light to the plasmon mode in NW [7]. Exciting SPRs are more effective at the bulged section, resulting in a stronger bolometric effect compared to the rest of NW.

Next, we examined the junction of metallic contacts and the NW, which causes a considerable negative photoconductance. The signal can be observed over the

7

contact and intensifies by approaching the junction (marked by the green box in Figure 2.2c). The intensified signal hints that naturally formed gaps at the NW and metal contact result in plasmonic heating. The mechanisms for the photocurrent generation over the electrode region will be discussed in the following.

To explain the observed signal over the metal electrodes, we propose that the SPPs excited at the indium contact surfaces can reach the Ag NW and indium junction. Heat generation at this localized hot spot produces a bolometric response. Plasmon creation needs matching between the momentum of the plasmon in the metal contact and incident beam. The incoming electromagnetic wave of the incident light excites plasmons through scattering at the rough surface of the indium needle, as shown in Figure 2.2f. The created plasmons propagate to the junction and resonate there. Ag NWs have a high temperature coefficient of resistance, which causes a bolometric response when junction temperatures rise. The laser power we used in SPCM measurement is relatively low. However, the plasmonic enhancement at the hot spot can raise the temperature by tens of Kelvins locally and generate measurable negative photoconductance.
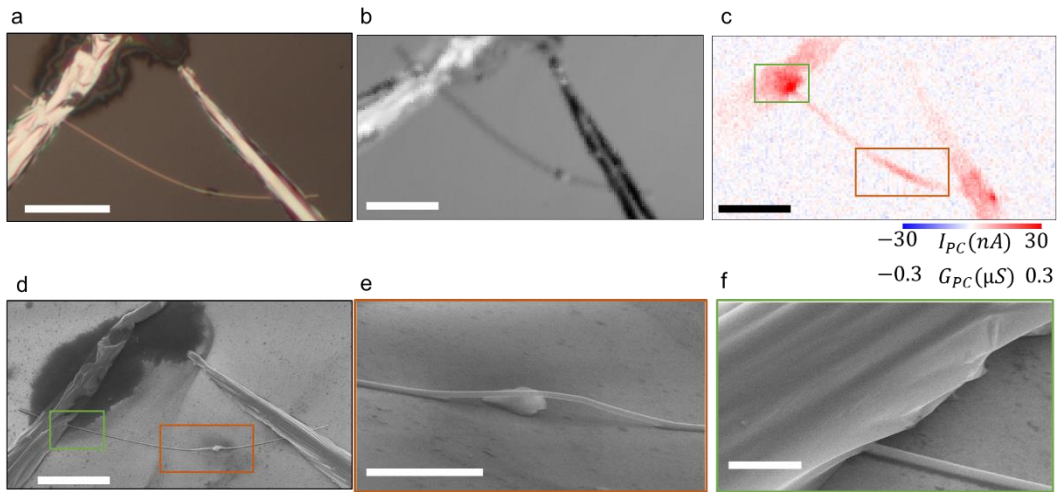
Figure 2.2: (a) optical microscope image. (b) reflected intensity map using 100μW, 532 nm laser. (c) SPCM map under 100 mV bias. We observed a more significant photocurrent signal at the NW-indium junction and bulged section of NW. (d) SEM image of the device. (e) SEM image of the bulged section of NW showed a stronger signal in the SPCM map. The deflection in NW breaks the geometrical symmetry

8

and excites more plasmons resulting in more heat. (f) Zoomed SEM view of the indium contact-NW junction. Localized surface plasmons enhance heating at the space between NW and indium contact. Also, the grating structure forms on the indium contact by solidifying melted indium. The effective scattering mechanism of the grating structure intensifies Light coupling to the plasmons. Scale bars in (a), (b), (c), and (d): 10 μm and (e): 3 μm and (f): 1 μm

To fabricate bottom contacted devices, we drop cased a dilute Ag NW suspension (0.02 wt. %) on the pre-pattered gold electrode. The NWs randomly dispersed between the pads, and then we located the devices which formed by a NW connecting two gold pads. The reflection images a bottom gold contact device is shown in Figure 2.3a. We measured considerable photocurrent under 20 and -20 mV bias on the gold contact pads, and the signal increases when the laser approaches the NW and contact junction. As can be seen from the SEM image, there is a gap between the two metals (marked by a dashed green box), which enhances the SPRs generated at the gold surface. A significant signal is produced due to resonating localized plasmons at the gap region. The gaps were also observed in indium contact-NW junctions depicted in the SEM micrograph of Figure 2.2f. Similar enhancement behavior in the photoconductance signal at the intersection of indium contact and NW can be seen from the SPCM map in Figure 2.2c.
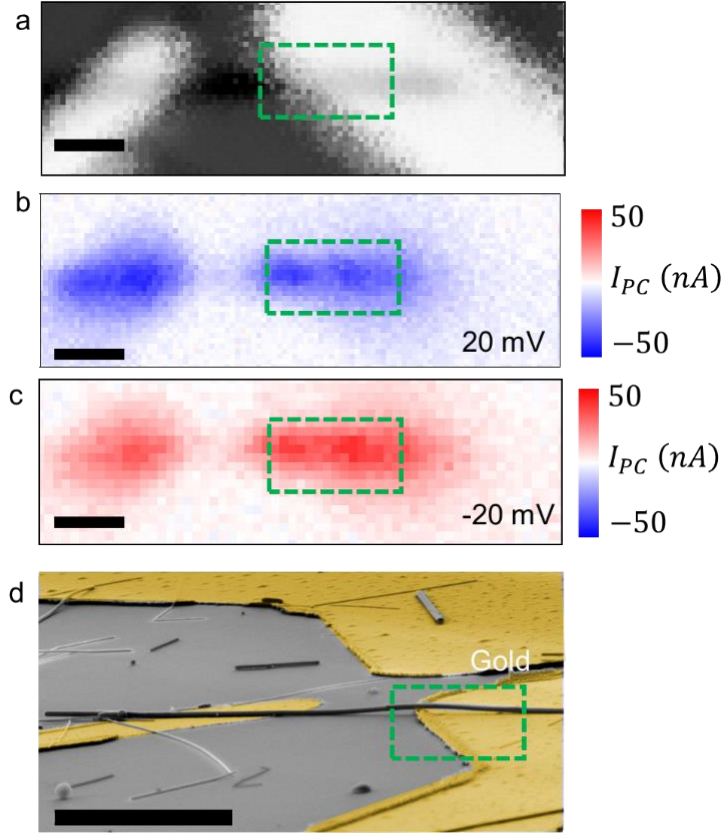
Figure 2.3: (a) the reflection map of the bottom gold contact device using 65 μW, 532 nm laser. (b) and (c) the photocurrent map under 20 and -20 mV bias. (d) the false-colored SEM image of the device. The tilted-view SEM image shows the gap between Ag NW and the pads. These local hot spots are responsible for enhanced signals in SPCM maps. The scale bars are 5μm.

By examining many devices, it became apparent that the contact resistance negatively impacts metallic NW photoresponse. Many devices at first cycles of IV sweeping show non-ohmic behavior with resistance up to MΩ. The IV curves shown in Figure 2.4b display the initial high resistance. After sweeping bias for 70 seconds, the device's resistance decreased and showed ohmic behavior (Figure 2.4c).

The poor electrical connection at the interface of NW and metallic contact causes an initial high resistance state. We didn't observe any photoconductance from devices showing resistance in the range of MΩ. During voltage sweeping, resistance drop in multiple steps to hundreds of ohms or less. Ag NWs have PVP insulating

coverage that is introduced in synthesizing process. Thus, welding the NWs to the contacts and each other is necessary to make an electrical connection with low contact resistance. Dropping in the resistance value in multiple steps shows that the dielectric barrier, PVP, is removed from the junctions due to joule heating. After a considerable reduction in resistance, the IV shows a linear trend, and the resistance value remained constant at 164 Ω (Figure 2.4c). We kept the bias voltage below 10 mV to preserve the device for the SPCM measurement. It is reported that bias voltages around 1V initiate the electromigration of Ag atoms. Electromigration changes the device's resistance due to amorphization or fusing the NWs into contact or each other [8][9][10].

Relatively low constant DC bias voltages for a long time at elevated temperatures can change the resistance of the device. The heat generation in the plasmonic device is more robust at the hot spots. Therefore, the laser illumination during the SPCM measurement can affect the NW-contact junction. The SPCM maps in Figure 2.4d show the bolometric response at the junction of NW and indium contact, meaning that the junction temperature increased due to plasmonic heating. Before the SPCM tests, the resistance of a single nanowire device was 164 Ω. After 81 photocurrent mapping, the photoresponse disappeared, and the resistance decreased to 37 Ω (Figure 2.4e). The noticeably lowered resistance demonstrates that fusing the contact metal to the Ag NW reduces the device's contact resistance.
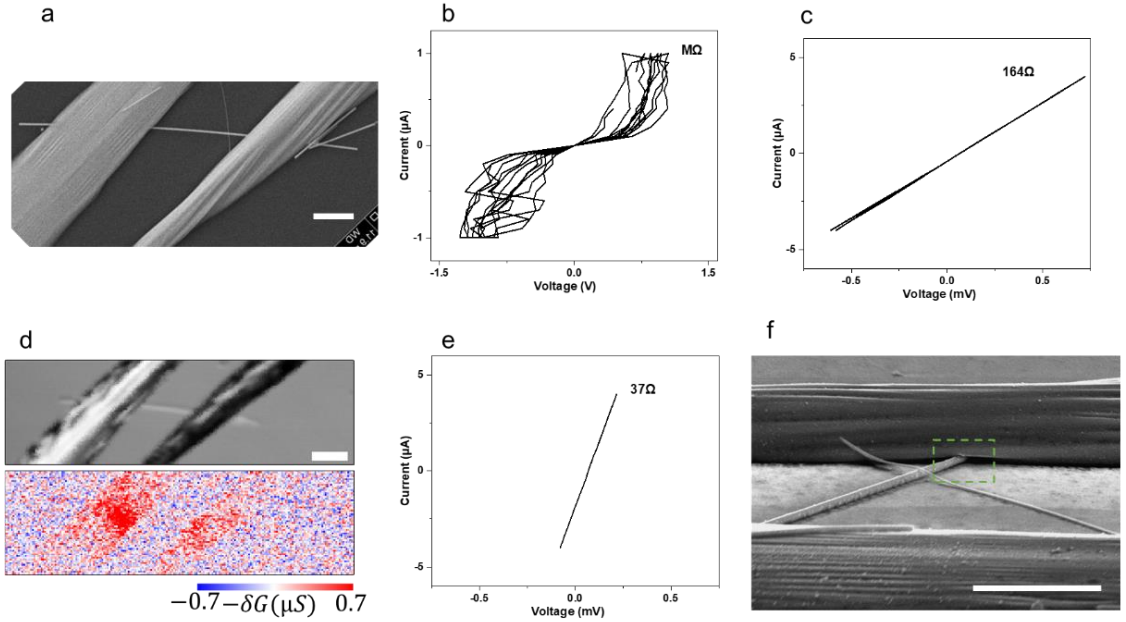
Figure 2.4: (a) SEM image of the device. (b) The current vs. voltage graph shows the high resistance and non-linear characteristic (c) Resistance reduced to 164 Ω after sweeping voltage for a minute. Joule heating improves the contact by removing the PVP barrier at the junction of NW and contact. (d) the reflection and the SPCM map using 60 μW, 532 nm laser,under 20 mV. (e) The current vs. voltage graph obtained after SPCM showed a decrease in resistance (f) The tilted SEM image of the device. The signs of fusing can be seen in the green dashed box. The scale bars are 5μm.

Electromigration can induce a more severe morphological change of the NW, affecting the device's performance. The simultaneous effect of the electrical current and propagation of plasmons in the NW can be seen in SEM images in Figure 2.5. More than 70 SPCM maps under voltage biases up to 100mV are performed before taking the SEM images. We can observe deformation in the section of NW located between two contacts (Figure 2.5b). The whole NW is scanned by laser several times, however, only the middle part between the contact exhibit mass transportation. A more zoomed view in Figure 2.5b shows the NWs between the contract is divided into two connected wires, and the NW seems intact beyond the contacts (Figure 2.5c). This indicates that the electromigration of Ag atoms is active in the part of the device that DC current is passing through it.
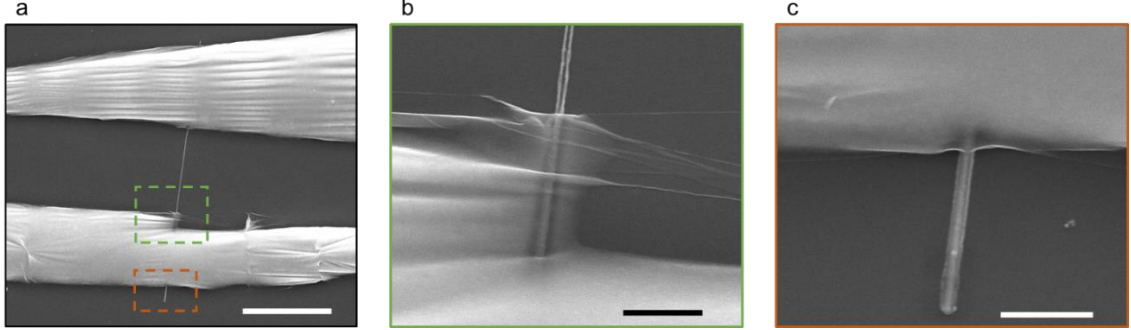
Figure 2.5: (a) SEM image of the device after 70 SPCM scans. (b) The zoomed view of the green dashed rectangle in the previous panel shows the splitting of the NW in the middle section. (c) The zoomed view of the orange dashed rectangle. NW morphology didn't show any splitting, as the applied current is not passing beyond the contacts. Scale bar in (a): 10μm, (b), and (c): 1 μm.

2.2   Photocurrent generation under zero bias

Here, we want to report the unexpected multiple sign change of generated photocurrent along the Ag NW at zero bias.

One of the fundamental characteristics of metal and semiconductors in thermoelectricity studies is the Seebeck coefficient. On the nanoscale, the Seebeck coefficient is highly sensitive to the electron mean free path which is affected by carrier density, impurities, temperature, and scattering mechanisms like surface scattering and grain boundary scattering. Variation in geometry and morphology affect the scattering mechanism and subsequently alters the mean free path. Therefore, the Seebeck coefficient is modulated by the changes in thickness, width, and surface conditions [11][12][13]. The photothermoelectric effect can be expected from Ag metallic NW when a temperature gradient is applied across the thermoelectric junction.

We should note that the bolometric effect is not at play as there is no bias applied to the device. The laser beam provides the temperature gradient required for thermoelectric response in the NW. Local heating elevates the hot region's

13

electronic temperature compared to its vicinity. As in the open-circuit configuration, no current can pass through the device. A temperature gradient develops a potential difference between contacts that prohibits the migration of hot electrons to the cold side [14]. This potential difference, known as thermoelectric voltage and can be obtained by

$$V = \int_{-l}^{l} S(x,T) \, \nabla T(x) dx$$

The S Seebeck coefficient varied by the location and local temperature, and ∇T is the temperature gradient due to laser heating. Due to simplicity, we perform photocurrent mapping rather than photovoltage mapping from the device. Using Ohm's law, we can relate photovoltage to the measured photocurrent. The similarity of the maps obtained by measuring photovoltage and photocurrent will be shown in the NW network section.

$$V_{PC} = R I_{PC}$$

$$I_{PC} = R^{-1} \int_{-l}^{l} S(x,T) \, \nabla T(x) dx$$

We observed the thermoelectric response in network, junction, and single NW devices. First, we focus on the Seebeck effect in a single NW because it has a relatively simple device structure. Figure 2.6 shows the SEM image, SPCM, and reflection map of the single NW device. Two 532 and 633 nm laser wavelengths were used to obtain the photocurrent map. The laser wavelength, power, and spot size determine the temperature gradient over the sample. Therefore, it is reasonable that photocurrent maps obtained by changing the illumination setup show different patterns. As can be seen from reflection and photocurrent maps in Figure 2.6b and c, the spatial resolution of the red laser is not as good as green one (Figure 2.6e and f). However, the alternation in the photocurrent direction is detectable using both lasers. We attributed the sign change of the photocurrent signal to the variation of the local Seebeck coefficient of the NW. A thermoelectric junction or "thermocouple" is formed at the junction of two materials with different Seebeck coefficients. As mentioned before, the defect, grain boundaries, and thickness

change can affect the Seebeck coefficient. It can be seen from the close-up SEM image in Figure 2.6g that the NW between the contacts has split into two parallel NWs, which are connected. The morphology, shape, and width of theses wire are changing along the NW, which can all modulate the Seebeck coefficient. The local variation of Seebeck coefficient forms a thermoelectric junction that generates photocurrent when it is heated. We should note the sign of Seebeck coefficient can be the same across the junction. However, the sign of Seebeck coefficient difference (ΔS) is different for the junctions showing opposite photocurrent directions. Considering a simple device model compromised from three regions with Seebeck coefficients of S1-S2-S1, the thermoelectric response at the junction of S1-S2 would has the opposite direction that the junction of S2-S1 as $\Delta S_{S2-S1} = - \Delta S_{S1-S2}$. The simulation results of a thermoelectric junction like this can be found in reference [15].
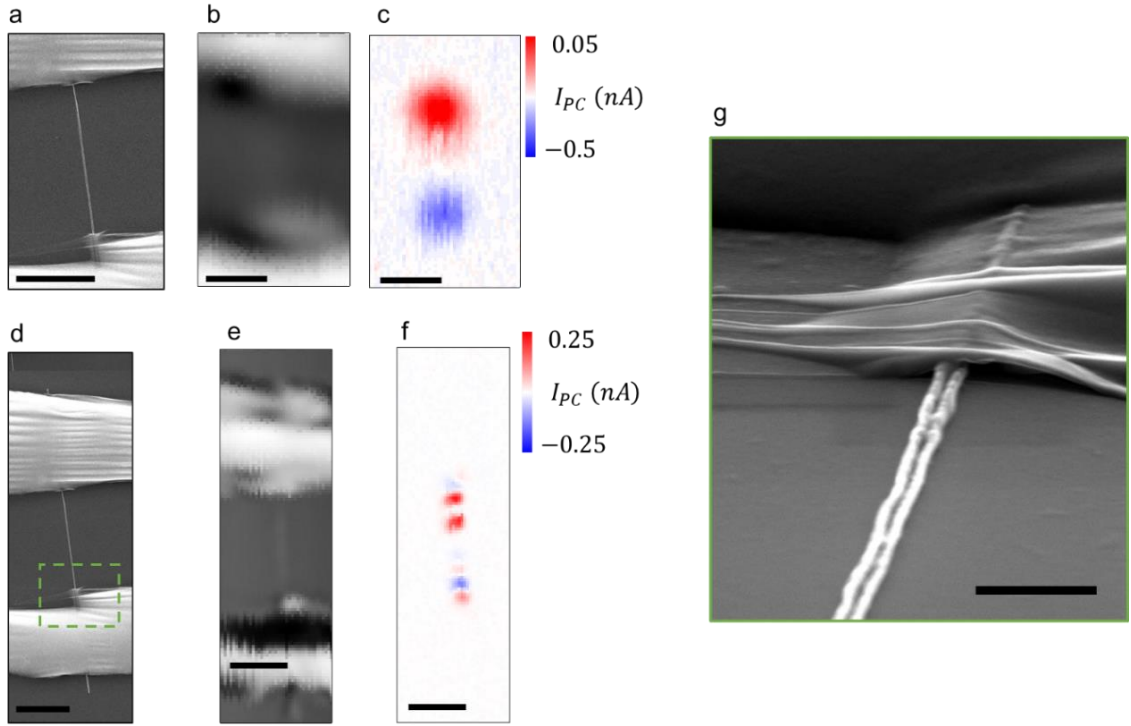
Figure 2.6: (a) SEM image of the device (b) The reflected intensity map using 96μW, 532 nm laser. (c) The SPCM was obtained at 0 bias using 633 nm laser. (d)

SEM image of device corrospond to the region in next panels (e) Reflection map using 100μW, 532 nm laser. The better image quality of reflection maps shows that the spot size of the 532 nm laser is smaller than 633 nm laser. (g) the zoomed view of the green dashed rectangle in the previous panel shows the splitting of the NW in the middle section. The variation in morphology causes Seebeck coefficient variation along the NW. Scale bar in (a), (b), (c), (d), (e), (f): 5μm, (g): 1 μm.

We also observed interesting and large photocurrent from devices containing a "nanogap". The nanogap is formed by applying enough large DC biases (or long-time low bias at high temperature) that causes electromigration. The plasmonic heating by the laser accelerates the formation of the gap structure. The current vs. voltage graph of a device before and after forming a nanogap is shown in Figure 2.7 a and b, respectively. The gap is formed after 10 SPCM mapping under bias voltages up to 100mV. Once a nanogap forms, the ohmic behavior of the device becomes non-ohmic, and the resistance increases from hundreds of to MΩ. Figure 2.7c shows the gaps near the junction. Nanogaps formed by Ag atoms electromigration are optically and electrically different from the exploded Ag NW devices. The size of a nanogap is in the range of a few nanometers, and current can still pass through the gap by direct metal-metal tunneling [16][17].
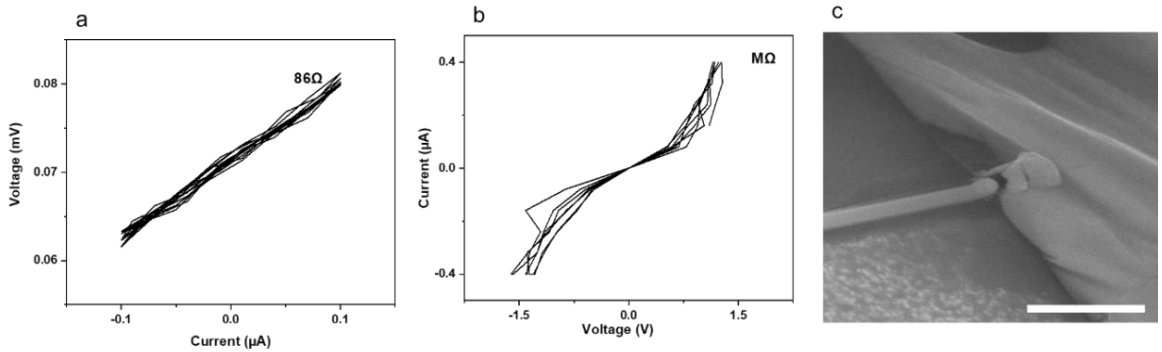
Figure 2.7: (a) and (b) (a) The current vs. voltage graph before and after SPCM scans. Nanogap formation increases the device's resistance to MΩs. (c) SEM image of the nanogap. The scale bars are 1 μm.

Figure 2.8a and e show the optical images of two single Ag NW devices, taken after performing SPCM measurement. Before SPCM, both devices displayed ohmic behavior with resistance around 300 Ω. Green arrows point to the gaps that appeared after measurement. Both devices show extraordinary photocurrent from the gap region.

The SPCM and reflection maps are shown in Figure 2.8c and g. The color SPCM scale bar is saturated in the following two panels. None of the other Ag NW devices shows such strong photocurrent at zero bias. The local and significant enhancement in photocurrent generation is associated with the gaps. The plasmon resonance at nanogaps creates heating and subsequent high energy, hot carriers able to tunnel the nanogap [13]. As the conversation of plasmon to heat by resonance is very efficient at the nanogaps, most plasmonic waves generated on the sample can cause the temperature gradient needed for the thermoelectric effect.

This result agrees with the previous study shows 1000 enhancement of the photovoltage compared to device without gaps [13]. Due to the widening of the gap size by excessive heat at the nanogap, further SPCM mapping was not possible. Deliberately fabricating the nanogap structures in Ag NW and controlling the gap's geometry requires further experiments.
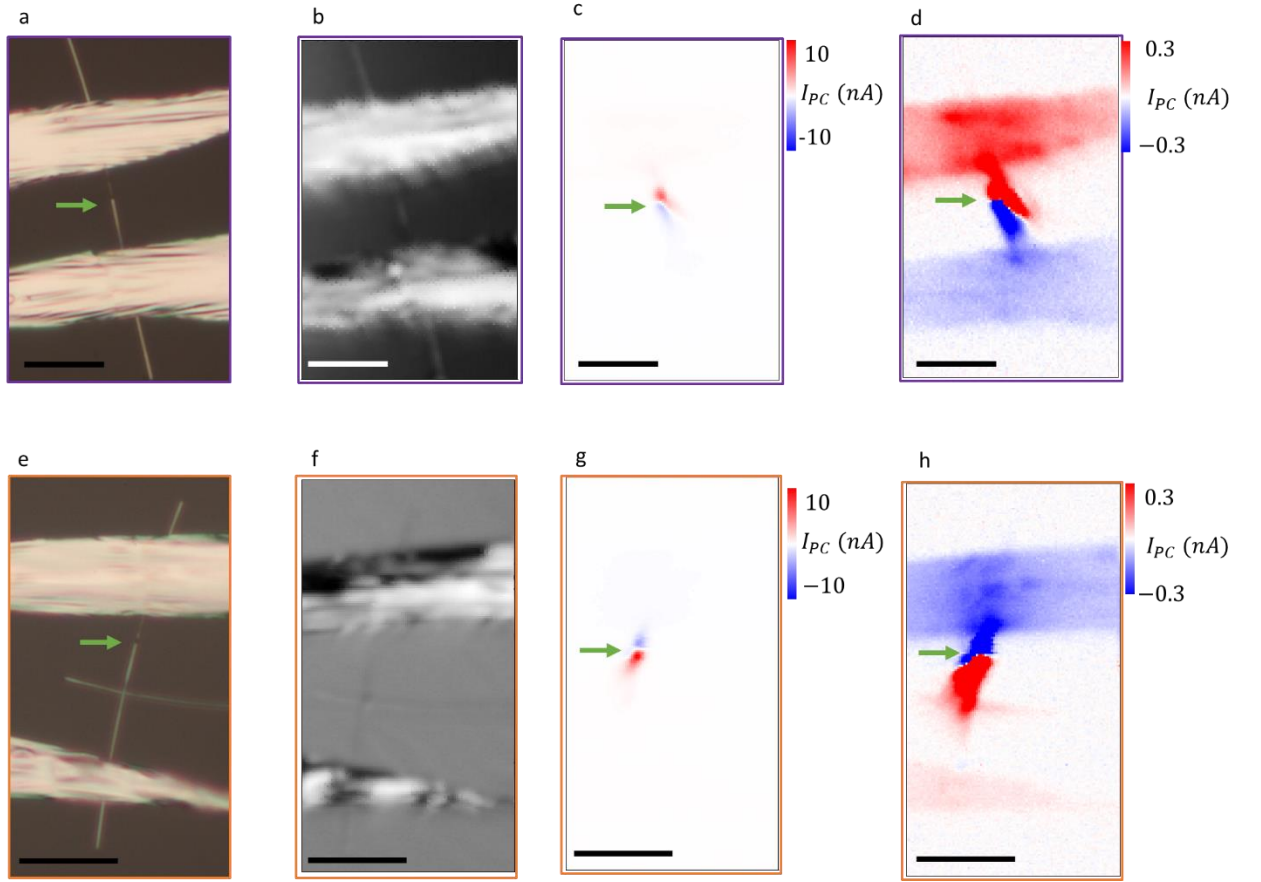
Figure 2.8: (a) and (b) optical microscope images of single Ag NWs devices. (b) and (f) The reflected intensity map using 100 µW, 532 nm laser. (c) and (g) The SPCM maps obtained under 0 bias voltage show a strong thermoelectric signal from the nanogap, pointed by the green arrow. (d) and (h) Color scale bar is saturated. Excited plasmons on the contacts and Ag NW propagate into nanogap and generate a significant photocurrent signal. Scale bars are 10µm.

2.3   Junction of NWs

As the most significant photocurrent comes from the junction site, we fabricate devices containing just one junction to analyze their photoresponse in more detail. Figure 2.9 shows the optical microscope image, reflection map, and corresponding photocurrent (and photoconductance $G_{PC} = \frac{I_{PC}}{V}$) maps from the NW junction device. Under zero-bias condition, no detectible photocurrent signal was observed.

18

However, the SPCM maps, obtained by applying 10 and -10mV bias voltage (Figure 2.9c and d), display negative photoconductance along the NW. The SPCM is quite similar when negative and positive applied bias, just the polarity of the produced signal is reversed. In other words, the increase in resistance due to laser heating and subsequent bolometric response is independent of the polarity of the applied bias.
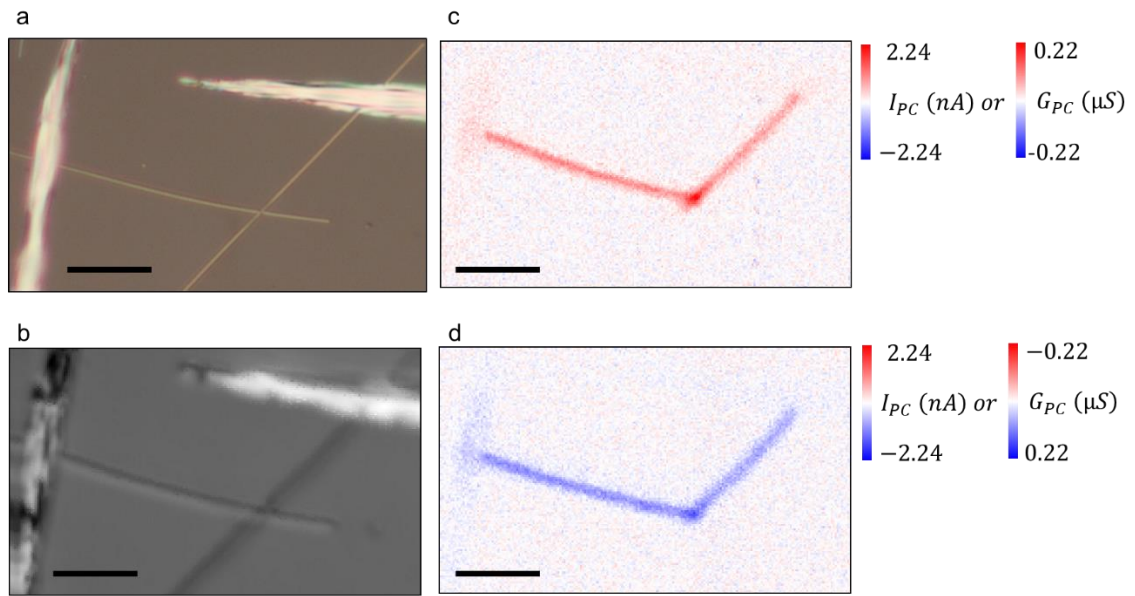
Figure 2.9: (a) optical microscope image of Ag NWs junction device and (b) The reflected intensity map using 53µW, 532 nm laser (c) and (d) The SPCM maps obtained under 10 and -10 mV bias voltage. Scale bars are 10µm.

Figure 2.10a shows the photocurrent along the black dashed arrow. The line trace graph reveals that the signal is intensified by approaching the junction, meaning that the junction affects the signal even when the laser spot is not on the junction. This behavior hints that the temperature rise is not just happening in the laser spot position. The propagation of plasmon to the junction and resonating there amplify the temperature rise at the hot spot junction. This mechanism

becomes more efficient by approaching the junction as SPPs travel a shorter distance.
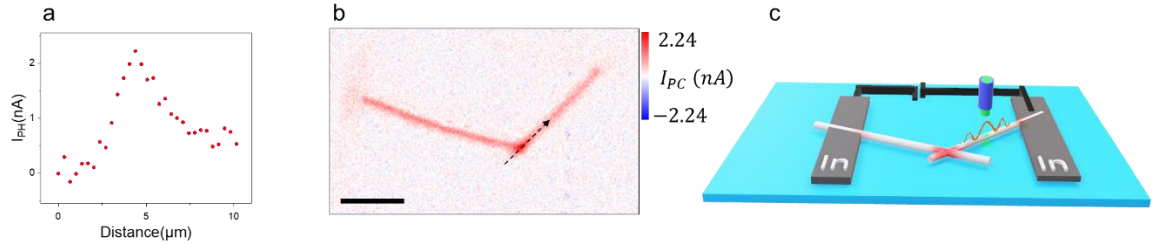
Figure 2.10: (a) The photocurrent along the arrow in panel (b). By approaching the junction, the photocurrent signal increases. (c) schematic of remote heating of the junction. Plasmon propagates along the NW and reaches the hot spot, causing a bolometric response in SPCM. Scale bars are 10µm.

Then, we studied the junction device depicted in Figure 2.11. The SPCM map at zero bias (Figure 2.11c) shows that the junction generates a positive photocurrent, and two points in the middle of NW exhibit the bipolar response. The bolometric effect cannot be considered as no bias is applied to the device. The inhomogeneity in the size of NWs is detectable in the reflected intensity map (Figure 2.11b). The local change in geometry, defect and overlaps of NW causes local variation in the Seebeck coefficient. The Seebeck effect is known to be the origin of the photothermoelectric at zero bias at metallic NWs Ref??.

The bolometric effect causes a negative photoconductance, as observed in SPCM taken with applying -10 and 10 mV bias (Figure 2.11). The interesting feature is that the signals are extended along the wire even after the overlapping NW junction at the open end of the NW. This observation is consisted with traveling SPPs along the NWs and raising the temperature at hot spot junctions.

The open circuit currents are added up to the bolometric response, visible in the photocurrent maps of the device under 10 and -10 mV bias. The zero bias response intensifies the signal if both mechanisms have the same polarity. The reversed polarity (pointed by the green arrow in photocurrent maps in Figure 2.11 d and e)

implies that the active mechanism in an open circuit configuration is stronger than the bolometric response under 10 and -10mV bias.
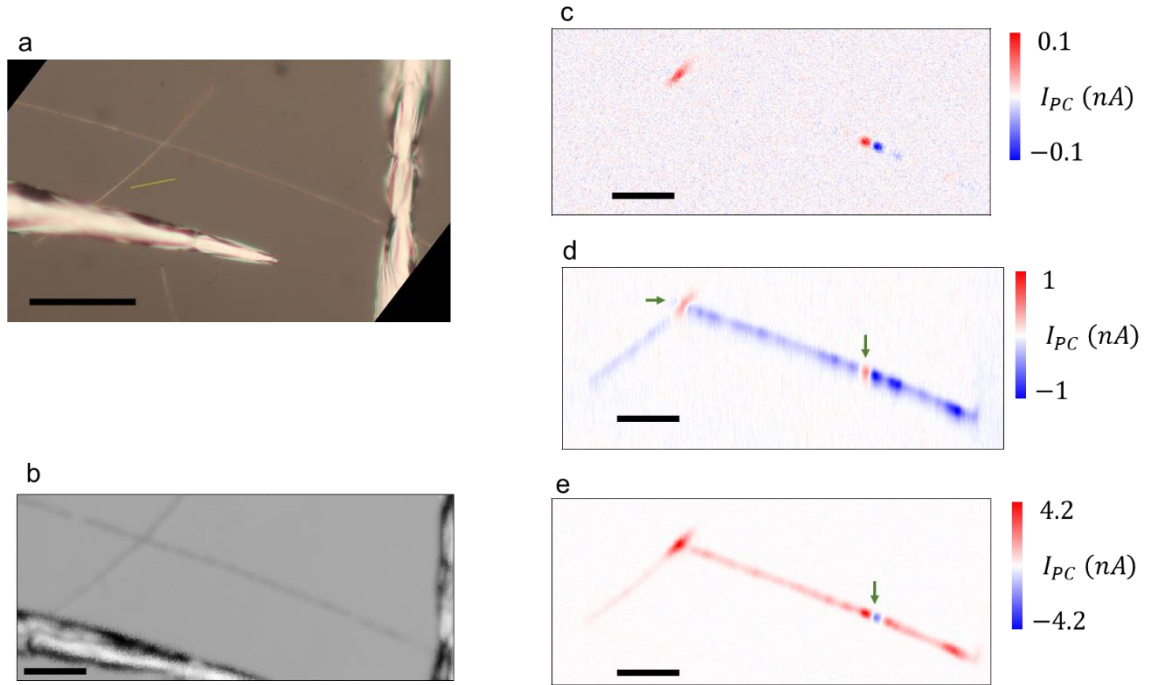
Figure 2.11: (a) optical microscope image of Ag NWs junction device and (b) The reflected intensity map using 50μW, 532 nm laser (c) and (d) and (e) The SPCM maps obtained under 0, 10 and -10 mV bias voltage, respectively. The photocurrent generated at zero bias contributes to the photocurrent map under bias. The reverse polarity of the signal pointed by the green arrow indicates that the Seebeck effect is the dominant mechanism there. Scale bars are 10 μm.

2.4   NW Network

W drop cast the 0.02 wt. % Ag NW suspension to form an Ag NW network device. Then we made contacts using indium needles (Figure 2.12a). The number of hot spots in the Ag network configuration increases due to NWs overlapping and NW-metal contact junctions. Figure 2.12b and c show the reflection and SPCM maps of the NW network device without applying any bias. The photocurrent is generated mainly at junction points of the network. The focused laser beam creates a temperature gradient by plasmon-assisted heating mechanism. As previously

stated in the zero bias response, morphological changes along NW and structural defects can cause Seebeck coefficient modulation. A thermocouple forms at the junction of two materials with different Seebeck coefficients. Heating this thermocouple by laser generates photocurrent at the network of NWs.
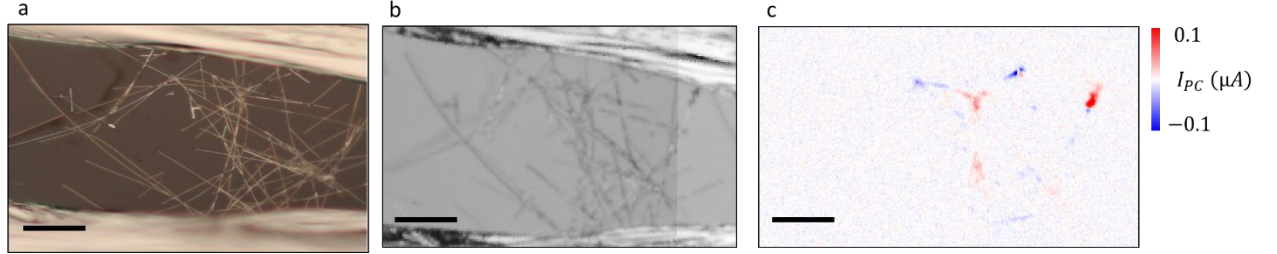
Figure 2.12: (a) optical microscope image of Ag NWs network and (b) The reflected intensity map using 100µW, 532 nm laser (c) The SPCM maps obtained under 0 mV bias voltage. The NWs junction and NW-indium contact junction generates photocurrent. The photocurrent changes by varying the Seebeck coefficient difference sign. Scale bars are 10µm.

The SEM image, reflection and photoconductance maps are shown in Figure 2.13. By applying a 100mV bias voltage to the sample, we observed a negative photoconductance along the NWs. Its magnitude increases in the vicinity of the junctions and shows a peak at the junction of two or more NWs. To investigate the dependency of photoconductance on bias voltage, we parked the laser on the junction and measured the photocurrent while sweeping bias. We chose the point that no photocurrent was detected in zero bias SPCM. The photoconductance is constant for different bias voltages (Figure 2.13e). Then photocurrent was measured while increasing the laser power. The graph depicted in Figure 2.13f shows a linear relationship between photoconductance and laser power. The linear relation is a good indication of the photothermal origins of the observed signal.

To elucidate the underlying mechanism of laser heating, we must first discuss the interaction of NWs with light, followed by the formation of hot spots. Metallic NWs support surface plasmons which are collective motions of the free electron at the surface of the metal and the dielectric environment around them.

The surface plasmons propagate along the NWs and finally release their energy by electron-phonon coupling to the lattice, which could raise the system's temperature locally. The heat generated by light absorption in plasmonic metals was initially thought to be a side effect, but using them as a heat source in the bolometry effect makes the NWs a promising photothermoelectric material in sensing applications. Capturing heat directly from SPPs on a single NW is difficult as the field enhancement around the nanowire is weak. Hence, the temperature increase would be small. However, hot spots are created by introducing a junction that naturally forms at the interface of plasmonic NWs. The amplified electromagnetic field at hot spots provides enough heat to modulate the device's resistance. The SPPs travel along the nanowire and resonate locally at the hot spot junctions, meaning that the temperature rise can be detected even when the hot spot is located remote from the illumination point [18]. Remote excitation distances beyond 10 μm are reported in the literature [7].

As can be seen from Figure 2.13c, a significant negative photoconductance on the indium contacts. The signal increases towards the NW-indium contact junction. Indium contacts are thick (1μm) and the laser power we used cannot raise its temperature directly by optical abortion. The optical absorption mechanism cannot provide a noticeable bolometric response from the indium needles. Local heating of the thick indium by laser is impossible. Still, the SSPs generated on the grating-like surface of indium are amplified at the hot spots, which are the naturally occurring gaps between the nanowire and indium contact surface. The enhanced plasmon heating at the hot spot junction is responsible for the signal observed from the metallic contacts.

We should note that the stability of the network devices was more than the junction device. In the network, many NWs can act as heat sink and regulate the heat before the excess heat can damage the device.
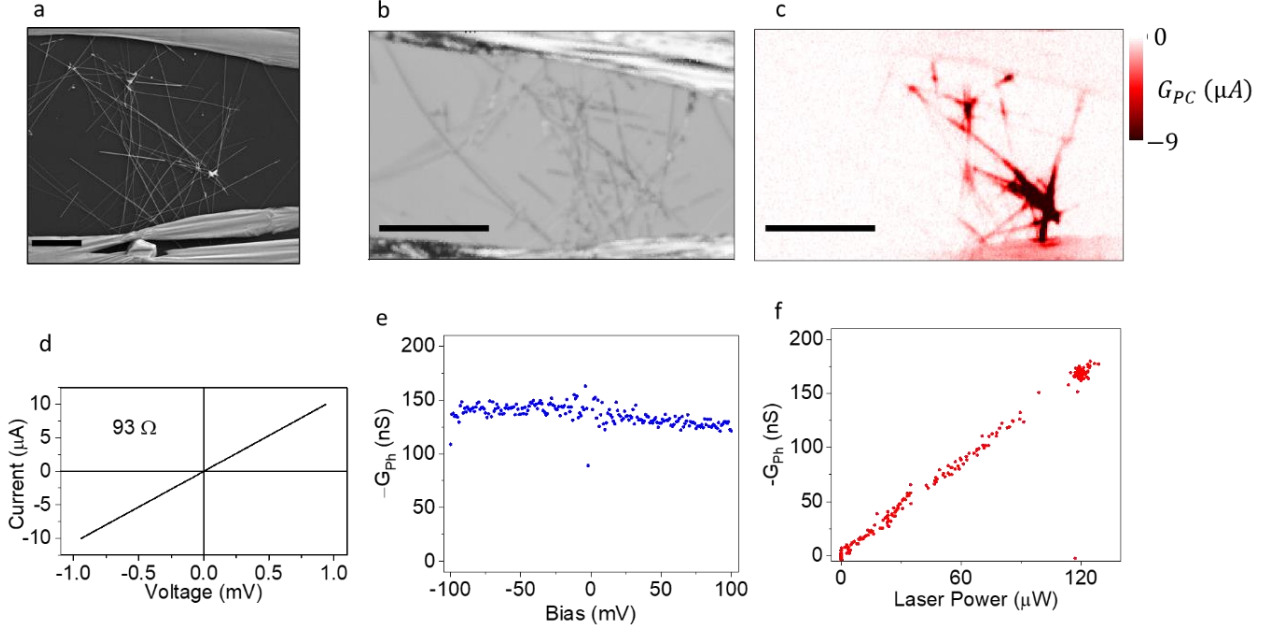
Figure 2.13 (a) SEM image of Ag NWs network. (b) The reflected intensity map using 100µW, 532 nm laser (c) The SPCM maps obtained under 100 mV bias voltage. Most Ag NW in the network shows bolometric response which peaks at the NW-NW junctions. (d) The current vs. voltage graph before SPCM scans shows ohmic behavior. (e) photoconductance vs. bias curve. Plasmonic heating increases the temperature of Ag NWs locally, causing resistance increase. The power laser is constant, so the heat that reaches the network is constant during the voltage sweep. Therefore, resistance change is independent of the applied bias. That's why the photoconductance is the same for the applied bias range. (f) photoconductance vs. bias curve. Scale bars are 10µm.

2.5   Polarization dependent plasmonic heating

We investigate the polarization dependency of the photoresponse in both bolometric and thermoelectric effects to illustrate the importance of SPPs in the heating process. We rotated the polarization angle of the excitation beam with respect to NW axis.

The schematic setup for controlling the polarization is shown in Figure 2.14a. The unpolarized light is not affected by a quarter-wave plate (QWP). Therefore, a linear polarizer is aligned to the light source to obtain high polarization extinction ratio. Then the linearly polarized light is converted to circularly polarized light by

a quarter-wave plate. The QWP divides the light into two electric fields with ¼ wavelength retardation, meaning that QWP produces circularly polarized light. The polarization is then controlled with a mounted linear polarizer. We measured the laser power at different polarization angles, shown in Figure 2.14b. Except for 330°, the laser power variation was less than 1%, meaning that the beam's intensity is the same for different polarizations. The photocurrent data are acquired from the SPCM maps, as the beam focus point might shift by changing the polarization.
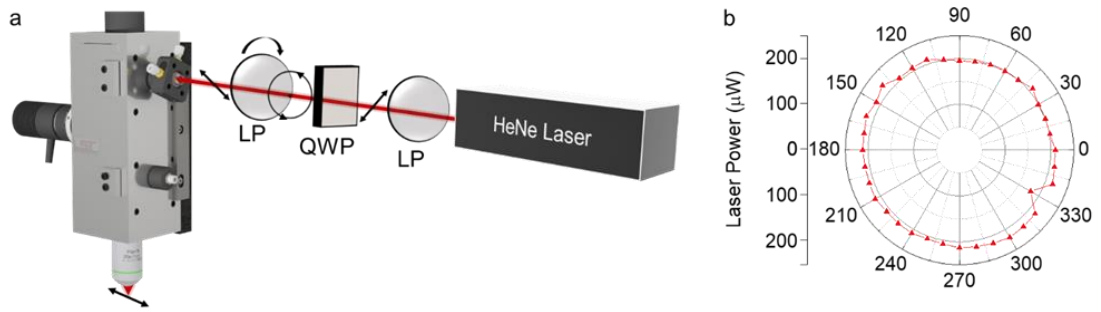
Figure 2.14: (a) Schematic of the polarization control optics. (b) Laser power vs. analyzer angle. The laser power is almost the same at different polarization.

Figure 2.15a shows the photocurrent map obtained using HeNe at 0 and 100mV biases at 0 polarization. We defined zero-degree polarization when the laser polarization is aligned with NW length. The SPCM mapping is obtained for different polarization angles and the averaged 9 pixels around the maximum signal were calculated. The green arrow points the maximum signal in Figure 2.15. The polar plot of the calculated value at different polarization depicted in Figure 2.15 b and d at 0 and 100 mV displays dipole character. The maximum photocurrent coincides when laser polarization is parallel to NW length, and the minimum happens perpendicularly. The photoresponse is highly dependent on polarization angle. Enhanced photoresponse in parallel polarization direction shows the significant contribution of the plasmon oscillation along the NW [19], leading to temperature increase. The laser power is almost constant at different polarization

angles (Figure 2.14b), meaning that the temperature raised by direct optical absorption of the metal is constant. However, varying the polarization affects the SPRs excitation, resulting in photoresponse dependency on the polarization angle [13] [11]. Interestingly, both 0 bias and 100 mV show the same trend of photoresponse to polarization angle, which implies the plasmonic heating origin in both Seebeck and bolometric effect.
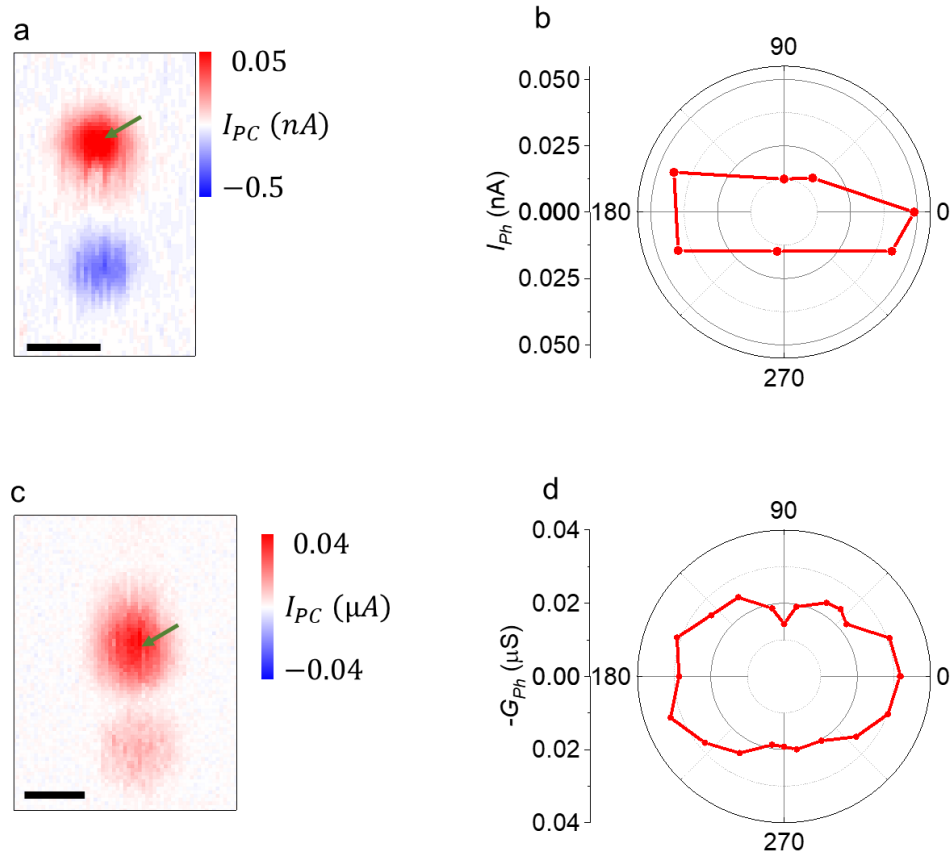
Figure 2.15: (a) and (c) The SPCM maps obtained under 0, 100 mV bias using 96 μW, 633 nm laser. (b) Photocurrent vs. polarization angle (d) photoconductance vs. polarization angle. Both polar polarization graphs show the maximum when polarization is parallel to the NW. Scale bars are 5 μm.

2.6   Raman Spectroscopy single NW and NW junction

We used Raman spectroscopy to characterize and study the light matter coupling in the single Ag NWs. The PVP characteristic Raman peaks were measured previously from the very dense and entangled area of the NWs [20]. Here, we report and discuss the Raman spectra and maps obtained from a single NW and the junction of two NWs. The scattering surface of a single NW is small. Therefore, the Raman signal is very weak compared to the dense area of the NWs. We kept the laser power below 70 μW to prevent damage to the NWs.

The Raman spectra of the Ag NW, depicted in Figure 2.16a, show the peaks at 1342 and 1590 cm^{-1}. These Raman peaks are related to polyvinylpyrrolidone (PVP) coverage over Ag NW. The Ag NW without polymer coverage is expected to be featureless in Raman measurements as the light penetration in metals is short due to metallic reflection, which makes scattering volume small. Also, most metals with BCC or FCC structures have no active Raman modes. A broad and low intensity peak in the range of 910 to 1060 cm^{-1}, is related to the substrate. By mapping the substrate peak, we can determine the exact position of the single NW. The black line in Figure 2.16c shows the single NW, as the NW blocks the weak signal from the substrate. The surface is mapped with the 1598 cm^{-1} peak intensity, related to the Ag NW, as shown in Figure 2.16d. Interestingly, both end of NW displays the signal, and no Raman shift is detected from the midpoints of the NW.
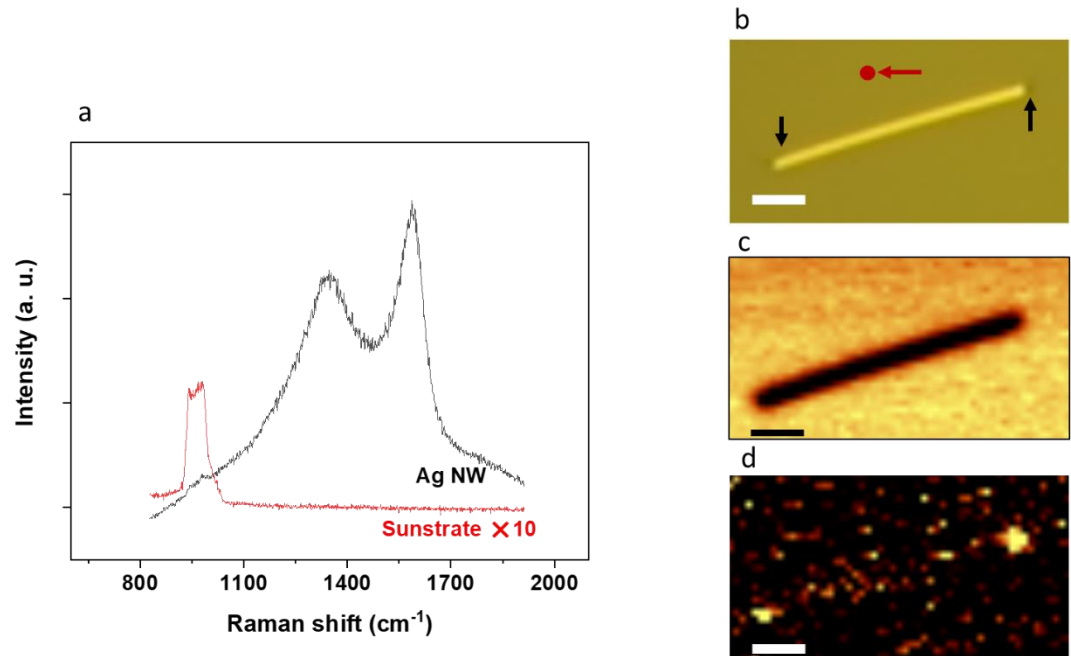
Figure 2.16: (a) Raman spectra from Ag NW endpoints and substrate. The intensity of the substrate peaks is increased 8 times to make it more visible. (b) optical image of the NW (c) the Raman mapping based on substrate peak. (d) the Raman signal was just observed from the endpoints, as the scattering mechanisms enable light coupling into and out of NW. Scale bars are 2 μm.

Then we studied the junction of overlapping NWs. Figure 2.17a show the optical image of three NWs that made two junctions. The broad and weak peak related to the substrate is used to locate the NWs in Raman map (Figure 2.17b). The NW pointed with the red arrow is thinner than the two other wires, and it couldn't remove the Raman signal coming from the substrate. Figure 2.17c displays the summation of the intensity of the PVP peaks. The most intense signals are located at the NWs junctions and endpoints.

As the thickness of PVP coating layer in NWs is a few nanometers, the enhanced Raman mechanisms are essential to detect a signal from the thin layer of PVP. Surface plasmon excitation can produce significantly stronger electromagnetic fields, which are the main enhancing elements in surface enhanced Raman scattering (SERS) method [21] [22]. The surface plasmons generate an

electromagnetic field that intensifies the Raman shift of PVP coating. In the following, we focus on how the scattering centers, like the end of NW and overlapping junctions or hot spots, cause this significant enhancement in the signal.

To couple the light into plasmons in metallic NW, their momentum should be matched. There is a momentum difference between the incoming photons (K Photons) and propagating plasmons (K Plasmons). The scattering sites can compensate the momentum difference and efficiently couple light into (and out of) plasmons by providing an additional wavevector (Δk Scatter). The scattering sites, like ends of NWs, defects and junctions between NWs or NPs break the symmetry and couple the light into propagating plasmons. The light cannot scatter at the middle part of NW because of the cylindrical symmetry over the laser spot area. Like absorption, the plasmon can reemit the light from the discontinuity sites. Discontinuities or overlapping of NWs are serving as both plasmon-lunching and emitting sites. The field enhancement by the surface plasmons is responsible for amplifying the signal from PVP at the ends of NW junctions.
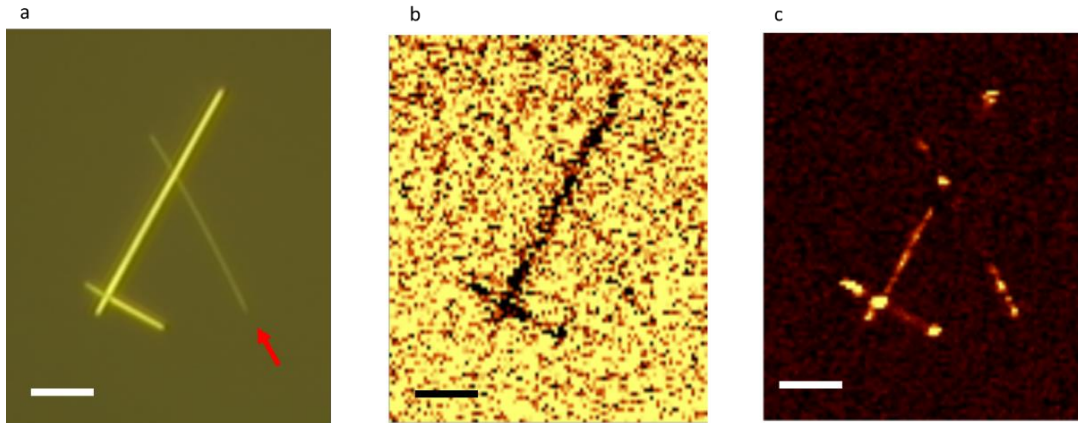
Figure 2.17: (a) optical image of the three NWs making two junctions (b) the Raman mapping based on substrate peak. (d) the Raman signals from NWs come from the NWs junctions and close to endpoints. Scale bars are 2 μm.

2.7   Decoration with Ag NPs

Decorating NW with nanoparticles can enhance the photoresponse in two ways. First, the presence of nanoparticles increases the coupling of the incident laser into plasmons, so more plasmons are created compared to the bare Ag NW [23]. Secondly, the interface between nanoparticles and NW forms a hot spot that enhances plasmonic heating. In a bare Ag NW network, the hot spots are located at the junction of the NWs and metallic contact. however, introducing the nanoparticle distributes the new hot spots all over the length of the NW. Creating more SPPs during absorption and introducing hot spots will generate more heat and intensify the bolometric response. To investigate the effect of NPs, single and network devices were fabricated, then the Ag NPs were drop casted to decorate the device. As seen from Figure 2.17, the NPs can distribute over the NW and substrate or form an agglomeration.
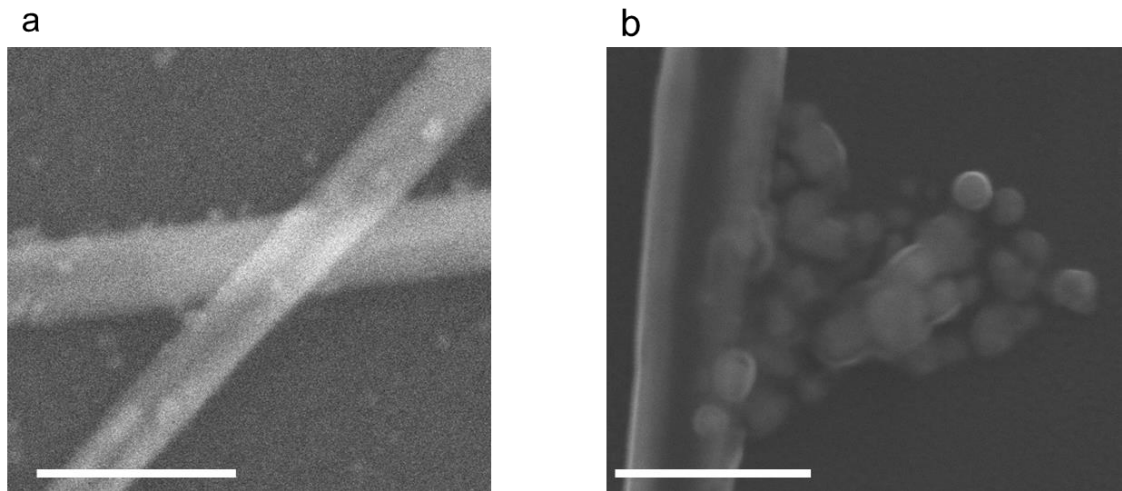
Figure 2.18: (a) well-dispersed Ag NPs on the Ag NWs (b) Agglomeration of NPs due to high suspension density. Scale bars are 300 nm.

Figure 2.19 shows the single Ag NW device with a junction in the middle and corresponding SPCM and reflection maps. The SPCM map in Figure 2.19c is saturated to show the features with lower intensities. The plasmonic heating that results from the field enhancement at the NW-NP junction spreads the response

along the entire Ag NW and considerably improves it. The negative photoconductance is more pronounced in the regions where NPs seem to be agglomerated point by the green arrow. The strong signal coming from the agglomerated Ag NPs is in consisted with the enhanced bolometric response by the gold NPs array [24].

As seen from the saturated SPCM map in Figure 2.19c, the part of NW beyond the indium contact display a bolometric response. Plasmons generated beyond the indium propagate to the hot spots and raise the junctions' temperature locally, resulting in bolometric response. The signal is enhanced because of the effective coupling of the light into SPPs by Ag NPs in the vicinity of NW. Also, the indium contacts show considerable photoresponse that intensifies by approaching the NW-contact junction. The grating-like structure of indium can excite SPRs traveling to the hot spot junction with NW and raise the temperature at the junction. The photocurrent on the indium contact increases as the distance that SPR travels becomes shorter. The observed signal beyond the metallic contact and on the open-ended crossing NW indicates the remote nature of photoresponse.

The zero bias response of the device is depicted in Figure 2.19e. The alternating photoresponse is observed at the area where NPs are agglomerated, shown with a green arrow. The NPs increase the surface area and alters charge charier scattering, which affects the mean free path. Therefore, the Seebeck coefficient can be affected by the aggregation of the NPs on the surface. The thermoelectric junctions between regions with different Seebeck coefficients generate photocurrent at zero bias.
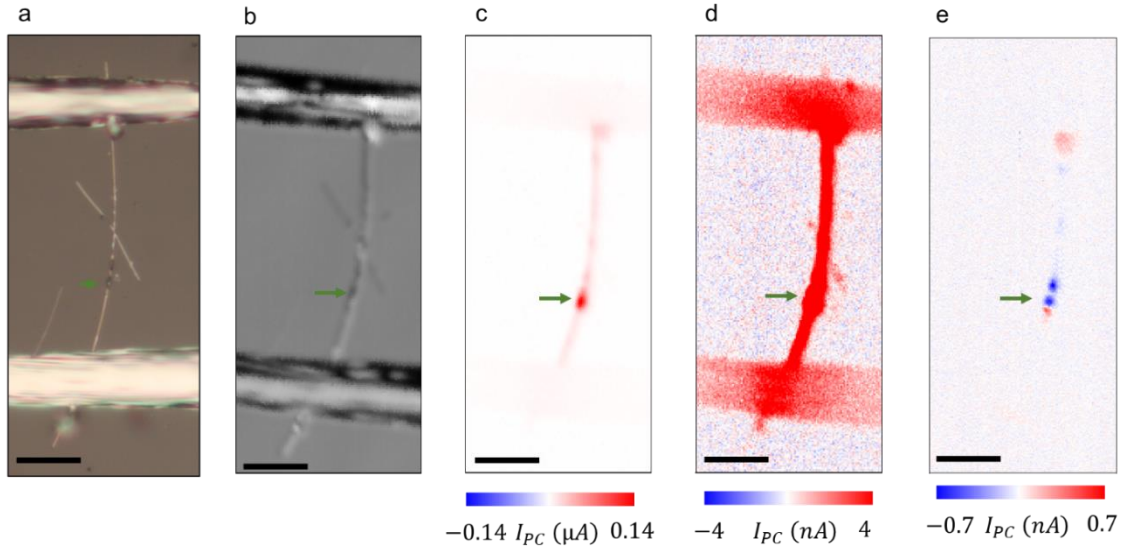
Figure 2.19: (a) optical microscope image of Ag NWs decorated with Ag nanoparticles (b) The reflected intensity map using 100 μW, 532 nm laser (c) and (d) The SPCM maps obtained under 100 mV bias voltage. A strong signal was detected from the nanoparticle agglomeration pointed by the green arrow due to enhanced heating by localized surface plasmons. The saturated SPCM map shows photocurrent beyond the contacts, revealing the remote nature of the plasmonic heating. (e) photocurrent generation under zero bias. Agglomeration of nanoparticles causes a thermoelectric signal. Scale bars are 10 μm.

We should note that the response of single NWs devices decorated NPs were not stable after several SPCM mapping. Figure 2.20a and b show the optical images of the device decorated with NPs before and after 15 SPCM mapping under bias. The points indicated by the green arrow are created by aggregation and melting the Ag NPs, making a micrometer-sized particle. The successive mapping from a single NW device with different bias are depicted in Figure 2.20d, e and f. The maximum signal shifts from upper to lower contact after 13 SPCM mapping due to Ag atom electromigration and melting NPs. The SEM image in Figure 2.20c shows that NPs are merged and make a big particle, moreover, the diameter of the Ag NW changed after many scans. These features are formed during several SPCM scans, that's why the position of the maximum signal is moving. This process hints that the Ag atoms

electromigration is accelerated in the presence of excessive heating created by plasmonic NPs.
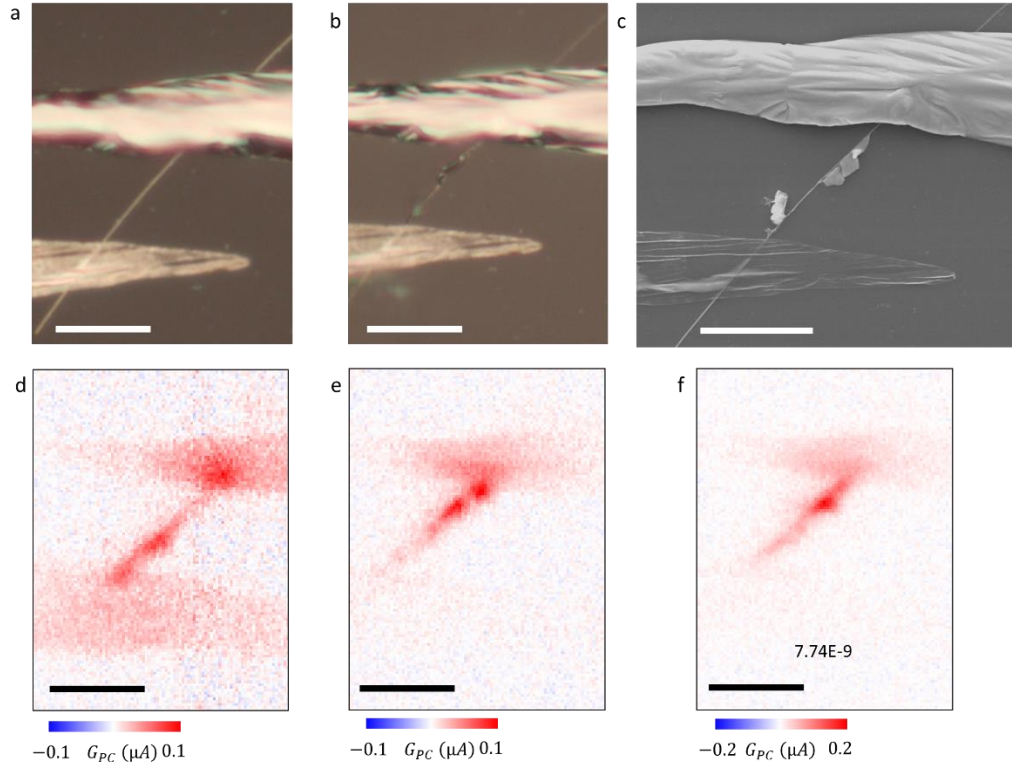
Figure 2.20: (a) and (b) optical microscope images of Ag NWs decorated with Ag nanoparticles before and after 15 SPCM scans. (c) The SEM images of the device after SPCM scans. The electromigration and fusing of the nanoparticles create massive Ag particles. (d), (e) and (f) the consecutive SPCM scans using 30 µW, 532 nm laser under 100, 40 and 40 mV bias. Due to morphology changes during scanning, the SPCM maximum signal is moving. Scale bars are 10 µm.

The morphological damages are mostly observed in single Ag NW devices. In the network devices, the current passes through a network of NW instead of a single NW, reducing the electromigration. Also, more heat conduction paths are available for heat dissipation before it can damage the network.

Decoration of the Ag network shows a similar photoresponse enhancement. Figure 2.21a shows the optical image of the Ag network devices decorated with Ag NPs. Ag NPs highly enhance the light coupling to plasmon, and almost all NWs

exhibit the photoresponse. As can be seen in Figure 2.21d, this response extended to the indium contact and beyond it. The significant and widespread signals indicate that hotspots are heated remotely by SPR reaching them. The NPs are well recognizable in the SEM image shown in Figure 2.21b obtained after measurement, and no sign of intense Ag atoms electromigration or NPs merging was observed. This indicates more stability and reliability of network Ag devices over a single NW device.
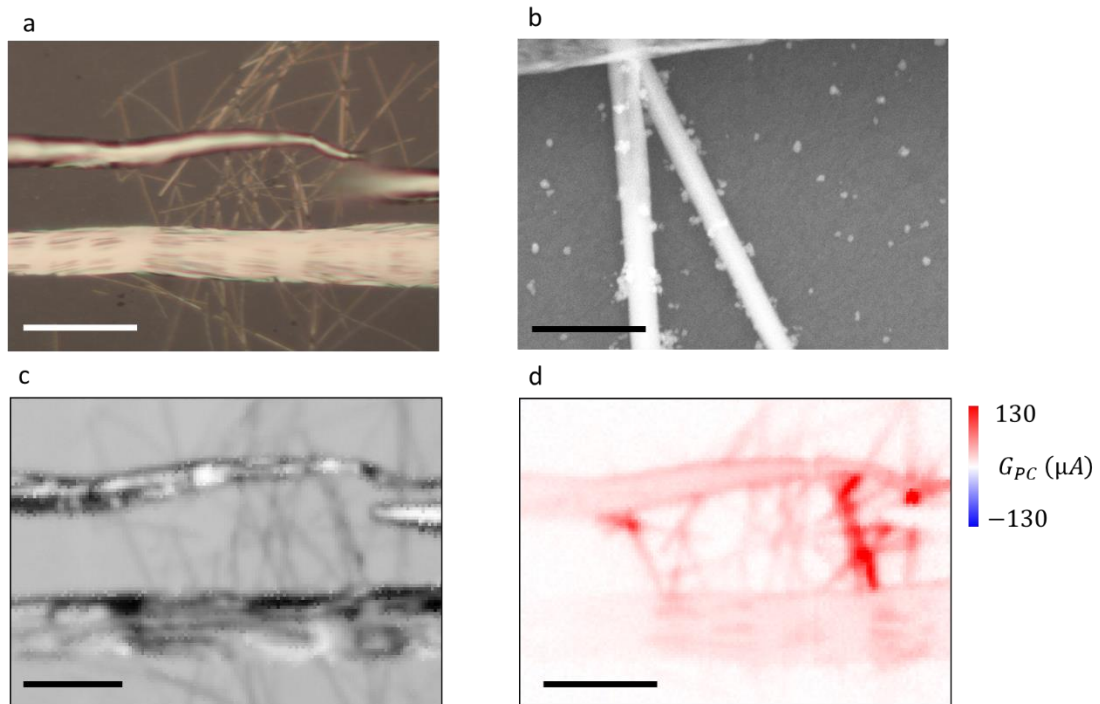
Figure 2.21: (a) Optical microscope images of Ag NWs network decorated with Ag nanoparticles (b) SEM images of dispersed Ag NPs over the Ag NW after SPCM scans. (c) The reflected intensity map using 93 μW, 532 nm laser (d) Photoconductance map under 100 mV bias. Scale bar in (a), (c) and (d): 10μm, (b): 500 nm.

2.8   Decoration with Quantum dots

In this section, we demonstrate the ability of a single NW device to absorb emission from cadmium selenide quantum dots (CdSe QDs). Previous studies showed that a large portion of QD's emissions is coupled to the SPR due to tight

field confinement in the vicinity of an Ag NW. Akimov et al. optically observed the scattered light at the end of NW comes from coupling the QDs emission into plasmon in NW [25].

The bolometric response of NW enables us to detect the SPRs created by QDs emission electrically. We first fabricated a single Ag NW device and then drop casted the QDs on the substrate. The optical image of the device and SPCM map is shown in Figure 2.22a. QDs are located on the NW and aggregated on the substrate in the vicinity of the NW. Based on the absorption and photoluminescence spectrum shown in Figure 2.22b, the absorption peak is located around the green laser used in this experiment. The strong negative photoconductance is measured from the NW in the circuit and the one crossing the NW. When the QDs are located within the evanescent surface plasmon tail, the NW can capture most of the radiation into plasmons due to the tight field confinement.

Also, QDs can directly emit the light that couples into plasmons in Ag NWs [19]. The aggregated particle far from the NW is pointed with the green arrow in SPCM and optical and scanning maps. The saturated SPCM map shown in Figure 2.22e reveals the photoconductance when laser scans the aggregated QDs at 10 μm distance from the conductive path of the device. The distance between the responsive QDs and the device is much larger than the laser spot size. This observation indicates that QD's optical emission is absorbed by Ag NWs, resulting in a measurable bolometric response. For further experiments, it is suggested that QDs place in more controlled ways using self-assembly methods.
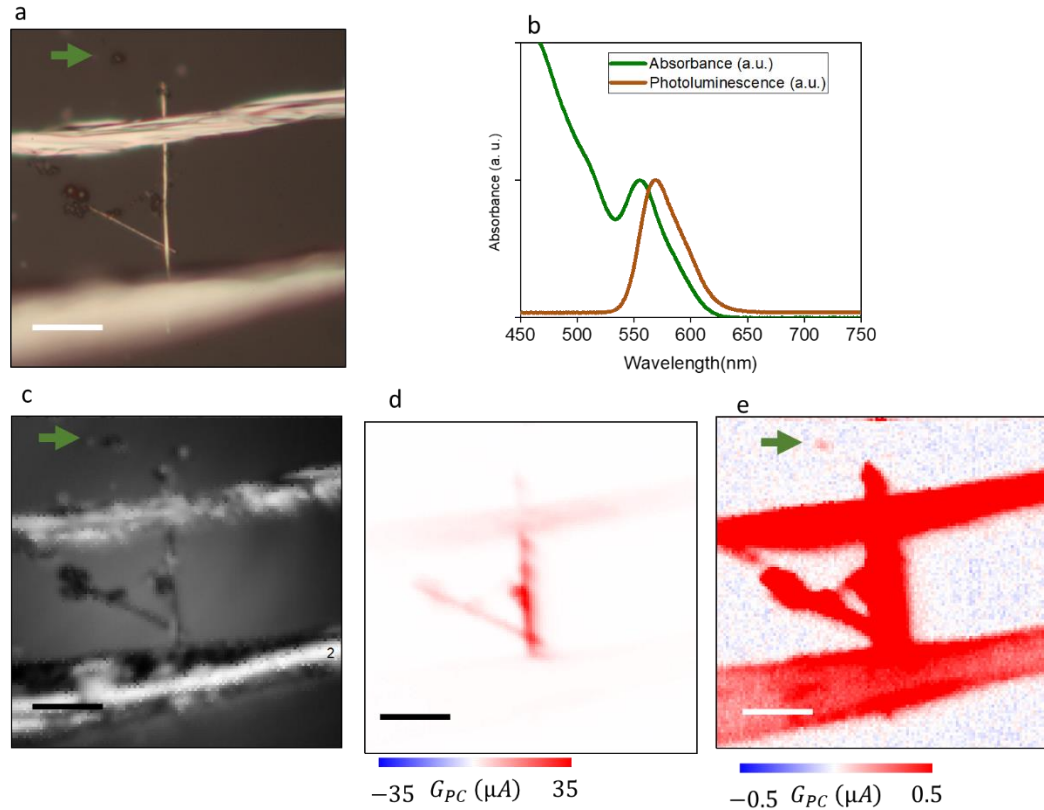
Figure 2.22 (a) Optical microscope images of Ag NWs network decorated with CdSe nanoparticles (b) (c) The reflected intensity map using 106 μW, 532 nm laser (e) Photoconductance map under 100 mV bias. (f) Saturated color scale bar Photoconductance map. The signal observed from the CdSe located far from the NWs and the contact due to emission and reabsorption by the NW device. Scale bars are 10μm.

2.9   Conclusion

We measured the photoresponse from the single NW and NW networks. We attributed the photoresponse to the bolometric effect for a device under bias. Plasmonic heating raises the temperature locally, which results in a resistance increase. At zero bias, the changes in the thermoelectric junctions generate the photocurrent. Variations in morphology and thickness, nanogaps can change a Seebeck coefficient and make thermoelectric junctions along the Ag NW. We

emphasized the role of hot spots like NW-NW and contact-NW junctions in observed photocurrent. Finally, the bolometric response was amplified by the decoration of Ag devices with Ag nanoparticles and CdSe QDs.

Chapter 3

Photocurrent generation from substrate engineered few-layer MoS$_2$

The transition-metal dichalcogenides are a group of materials with MX$_2$ formula in which M represents a transition metal (Mo, W, Nb, Ta, Ti, Re) and X is Se, S or Te. Whit in the layer, The Metal atoms are sandwiched between two layers of X atoms. The layers are vertically stacked by week Van der Waals interaction between them, making it promising to obtain few and mono layers and study two-dimensional materials. Molybdenum disulfide (MoS$_2$) is probably the most studied material in this family, with a layer thickness of 6.5 Å, Mo and S strongly covalently bonded within the layers that bring it high strength and stability. Unlike zero band gap graphene, MoS$_2$ in the bulk form has an indirect band gap of 1.2 eV. The band gap energy changes with thickness or number of layers and becomes direct as it becomes a monolayer [26].

3.1 Exfoliation of MoS$_2$

The MoS$_2$ source contains big flakes and shiny crystals with centimeter dimensions. The exfoliation method is used for thinning the crystals up to a few nm thicknesses. First, the piece of flake is detached from the source and placed on the sticky side of the tape in a way that the flake is parallel to the tape surface. In practice, the master tape with many bulkish flakes is used as a source to produce a bunch of other tapes for the next step of transferring. Sandwiching the flakes between two sticky sides of tape will make the flakes thinner. This process needs the adhesion force between the tape and flakes to be less than the van der Waals force between the crystal layers. Repeating the exfoliation gives a thinner crystal.

It also breaks the crystal into small pieces, which is not useful for many device fabrication purposes.

3.2 The size estimation using an optical microscope

Before transferring the crystal, the optical microscope is the only way to find thin enough crystals for device fabrication as more accurate methods like AFM are not applicable on tape. Recently, Deep-learning based image processing is developed to determine the thickness of transferred 2D materials using optical microscope imaging as it is critical to find proper crystal [27]. In general, the thick crystals seem to have a shiny metallic reflection, while the thinner ones have a range of colors, and extremely thin crystals are barely visible with the microscope light. Lowering the microscope light provides better contrast between the thin crystals and the substrate and makes it possible to detect trapped air beneath them, as depicted in Figure 3.1a. The trapped air beneath the crystal is detectable using AFM, and it contributes to the photocurrent signal. We tried to select as much as possible thin crystals, without any mechanical damages like folding and cracks in the region of our interest. Crystal thickness used are between 2nm to 14nm measured with AFM.
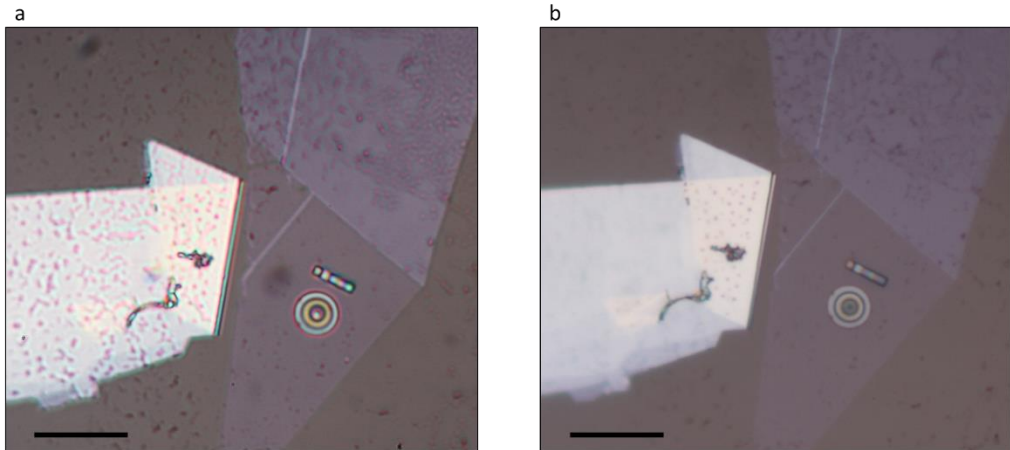
Figure 3.1: (a) and (b) Optical images of transferred MoS_2 on the sapphire substrate under low and high light intensity, respectively. The surface of MoS_2 is not flat and

some bubbles are formed after transferring. The rectangle and circular hole milled with FIB to partially suspend the crystal. The scale bars are 10μm.

The lifetime of the MoS_2 device is quite long. After more than six months, we checked some devices, and they showed similar photocurrent behavior. Some of the samples were annealed in CVD chamber for 4 hours. No significant changes are observed in the photocurrent signal of the annealed and as-prepared sample in the region of our interest, the junction of the supported and suspended parts.

3.3   Metallic Contacts

To achieve high-efficient electronic and optoelectronic devices, it is critical to make clean Ohmic contacts at the interface of metal and semiconductors. Conventional patterning and metal evaporation process produce defects in MoS_2 crystal because of the invasion of the evaporated metal to the surface of 2D material. The atomic defect and crystal disorder in 2D materials causes defect-induced gap states, leading to Fermi-Level Pining at elevated temperature and increasing contact resistance [28]. From this view, indium is a more suitable candidate for metallic contact as its evaporation temperature of the indium is 300 °C lower than gold case.

Figure 3.2a shows a MoS_2 device that contacts deposited by indium evaporation. As can be seen from the zoomed view in Figure 3.2b, the evaporation of indium makes a non-uniform surface which can increase contact resistance. Cooling the stage holder up to 100 K in the evaporation process is employed to avoid this nonuniformity in surface morphology [28]. The liquid-nitrogen cooling process inside the evaporation chamber can produce clean Ohmic contacts, but lithography and evaporation steps can damage the suspended part of the sample. To overcome all these device fabrication issues, we fabricate our device by drawing indium needles on devices. By drawing melted indium using a tungsten needle, we can make devices with channel lengths as small as 4 μm. Since indium has a low melting point (156

°C), MoS$_2$ crystals can be preserved at this temperature. The typical contact configuration is shown in Figure 3.2c and d.
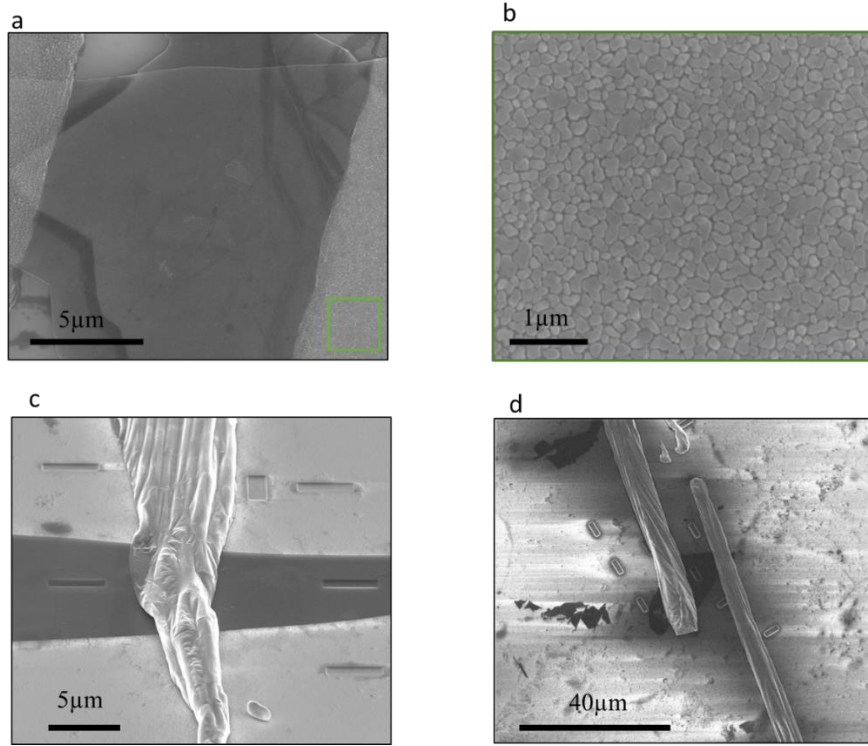
Figure 3.2: (a) SEM image of a MoS$_2$ device in which contacts are fabricated by the indium evaporation (b) The zoomed SEM images from the indium contact area marked by a green rectangle in the previous panel. (c) and (d) Typical indium contact devices made by drawing melted indium.

3.4   Transferred MoS$_2$

To study the substrate-effect on 2 dimensional materials, we transferred the MoS$_2$ to the substrate with holes or trenches. The holes on the substrate are milled using a Focused Ion Beam (FIB). To prepare the holes or trenches, 30nm of Chromium is coated on SiO2 or sapphire substrate to make the substrate surface conductive, which is needed for drilling the hole and trenches using FIB. Figure 3.3 shows an SEM image of a trench structure with a depth of 200nm before transferring the crystal. The chromium layer can be easily removed by etchant after holes are made. The optically defect-free crystal on the PDMS is picked for device

fabrication and then transferred on top of the hole. The suspended regions of MoS_2 on the hole /trenches show different colors than the regions supported by the substrate, as shown in Figure 3.3b.
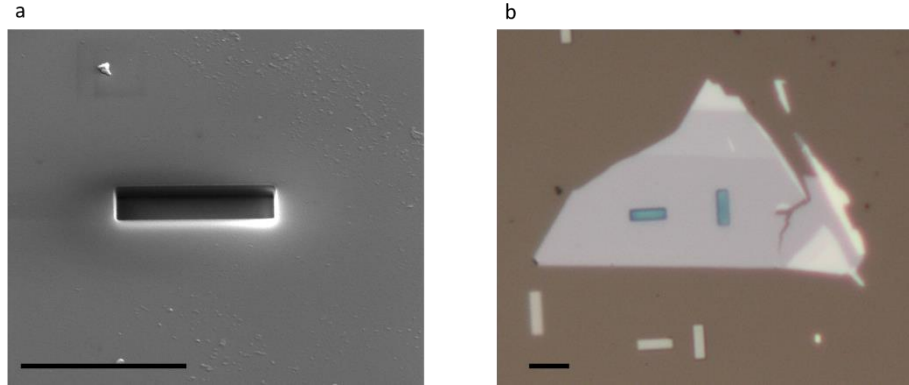
Figure 3.3: (a) SEM image of a trench milled using FIB. (b) the transferred MoS_2 on the substrate with trenches. The suspended part on the trenches shows a different color than the rest of the crystal. Scale bars are 4 μm.

The multiple trenches with varying depths from 100 nm to 600 nm also were drilled using FIB to study how the MoS_2 response changes when the separation between the bottom of the trench and flake alters. The SEM and optical images of a substrate containing trenches with different depths are shown in Figure 3.4. Different colors can be seen in optical images of transferred crystal results from different interference of the microscope light with the MoS_2 and outer surface of the trench/hole with varying depths.
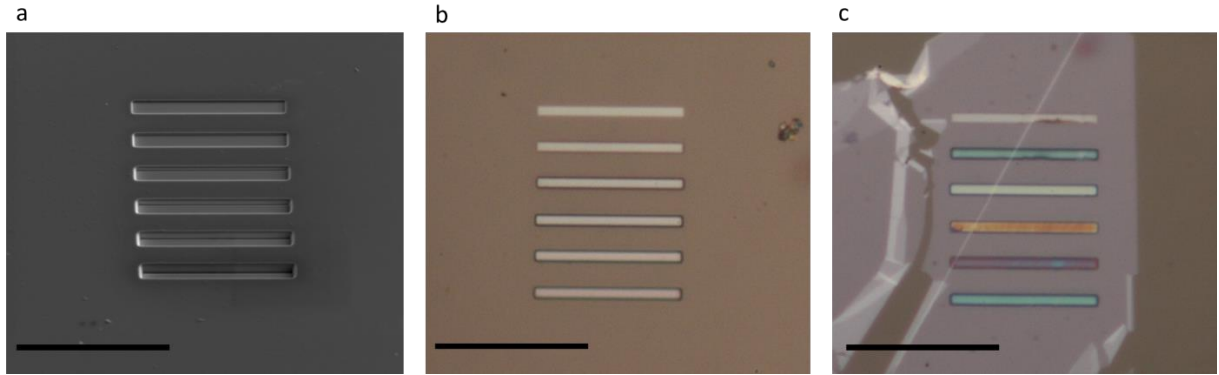
Figure 3.4: (a) SEM image of trenches with different depths milled using FIB. (b) optical image of the same trenches (c) the transferred MoS2 on the trenches. The suspended region color changes with respect to the depth of the trench. Scale bars are 10 μm.

We utilized Raman spectroscopy to investigate the substrate effect on the MoS$_2$ flakes. Two prominent peaks related to in-plane (E^1_{2g}) and out-of-plane (A_{1g}) around 385 and 405 cm^{-1} can be observed in the Raman spectra of MoS$_2$ depicted in Figure 3.5. The E^1_{2g} vibration includes the opposite direction motion of molybdenum and sulfur atoms. The relative out-of-plane motion of sulfur atoms makes A_{1g} vibrational mode. Both Raman modes exhibit redshift and increase intensity on the suspended region. So, Raman mapping is helpful in differentiating suspended parts from those stuck to the substrate or trench bottom.
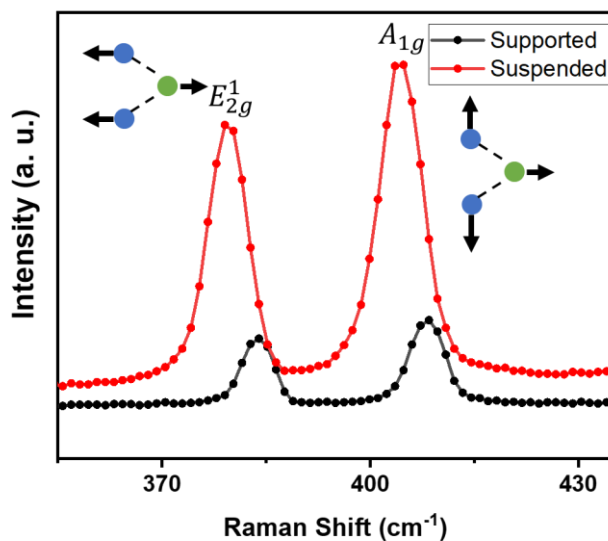
Figure 3.5: The Raman spectra from the suspended and supported MoS_2. The intensity is increased on the suspended region, and both peaks exhibit redshift.

Transferred crystal can either be stuck to the walls and bottom of the hole or suspended on the hole and trenches. Considering more than 60 samples, we speculate that in the samples with trenches/holes with depths less than 100 nm, MoS_2 can bend inside and stick to the walls. Trenches with staircase structure (Figure 3.6b) enable us to analyze the stuck and suspended parts in the same crystal flake. Figure 3.6 compares the optical images and Raman maps from suspended and supported parts by the substrate. The microscopic image showing the crystal colors stuck to the trench's bottom marked by a white rectangle, differs from the suspended regions. Raman shift and intensity maps with (E^1_{2g}) and out-of-plane (A_{1g}) are presented in Figure 3.6, obtained with 350µW laser power. Both characteristic Raman peaks of MoS_2 are highly sensitive to the presence or absence of substrate. The intensity of suspended parts is considerably higher than supported parts. On the other hand, the supported parts inside the trench (marked by white rectangle in Figure 3.6a, e and f) show similar or even lower intensity than the supported part, without any hole. The same intensity of the parts stuck to the

trench and the supported parts outside the trench indicate that the gap between crystal and substrate is crucial to observe Raman peaks shift and enhance their intensities.
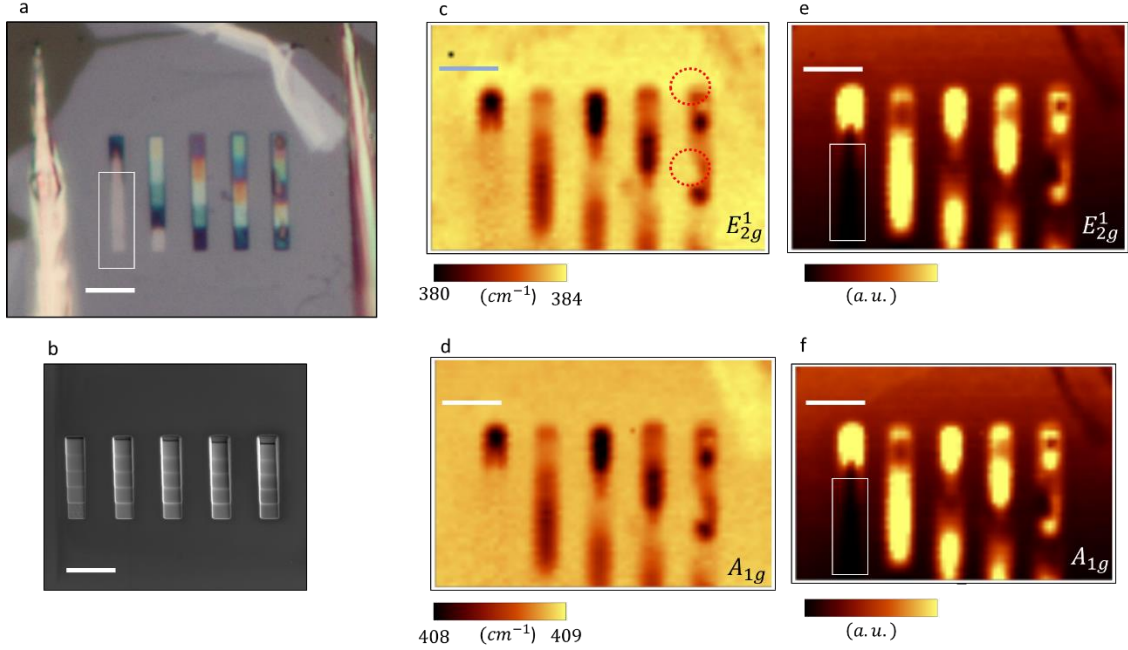
Figure 3.6: (a) Optical image of transferred MoS$_2$ on the staircase trench structure. Crystal stuck to the trench's bottom in the region marked by a white rectangle. (b) SEM image of milled trenches with the staircase structure. The depth of the left trench is smaller than the others. (c) Raman shift map of the E$^1_{2g}$ mode. (s) Raman shift map of the A$_{1g}$ mode. (e) Raman intensity map of the E$^1_{2g}$ mode. (s) Raman intensity map of the A$_{1g}$ mode. Both peaks exhibit redshift and higher intensity on the suspended part. The distance between the suspended crystal and the bottom of the trench affects the amount of redshift and its intensity. The scale bars are 4 μm.

In the following, we discuss strain, dopant concentration and temperature rise as possible origins of observed redshift in Raman peaks. The AFM map in Figure 3.7a gives a better vision of suspended and stuck parts of the staircase structure. The crystal stuck to the bottom of the leftmost trench, and its height increased as the staircase reached the surface. On the other trenches, the MoS$_2$ is suspended and showing ≈25 nm bulging up. As can be seen from the graph in Figure 3.7b, the

dashed black line trace shows a wavy pattern. The wave patterns are also detectable in other trenches in the height trace map and will be discussed later.
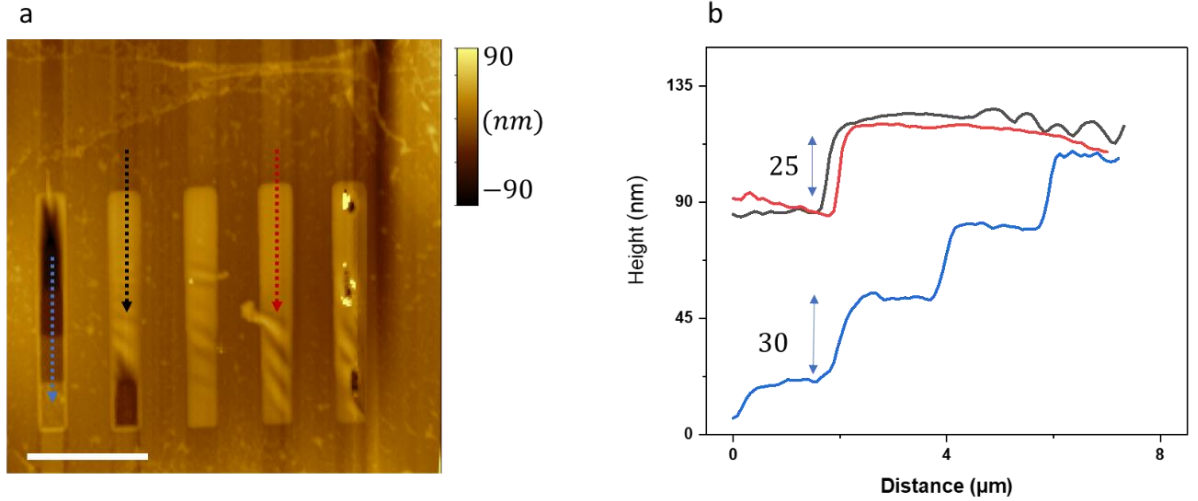
Figure 3.7: (a) AFM height trace map of the MoS$_2$. The crystal bends inside the left trench and sticks to the bottom due to the lower depth than the other trenches. (b) the height trace lines along the red and black dashed arrow show that the suspended parts are bulged up around 25 nm. Scale bar is 4 μm.

First, we examine the strain as an origin of the observed red shift in Raman peaks. Using Hencky's model [29], we calculated the biaxial strain at the center of a circular hole as

$$\varepsilon = \sigma(v)(\frac{\delta}{a})^2$$

$\sigma(v)$ is a constant depends on MoS$_2$ Poisson's ratio, for MoS$_2$ considering $v = 0.29$ gives us $\sigma = 0.709$. We accurately measured membrane deflection δ and membrane radius a with AFM. The suspended part of the hole forms a bulge with a height of 25nm. This value is similar to the MoS$_2$ transferred in the trenches. Using Hencky's model, the biaxial strain is calculated as low as 0.04 %.

The Raman shifting rates by strain are -1.7 cm^{-1}/% and -5.2 cm^{-1}/% for in-plane (E$^1_{2g}$) and out-of-plane (A$_{1g}$) vibrations, respectively. This minor strain, 0.04%, is not enough to cause a redshift in Raman peaks that we observed. The suspended part of the MoS$_2$ is in stress-free condition, experimentally and numerically shown

by Zhang et al. [30]. As a note, to impose a considerable shift in Raman peaks by strain, the pressure can apply to the membrane by introducing (depleting) the inert gas inside (from) the hole [29].

Isolating the crystal from the substrate also can affect the doping level. We expect that the doping should not be affected by the depth of the trench, meaning that MoS_2 must have the same doping level along the suspended region. As can be seen from Raman Figure 3.6c, both peak position and intensity are strongly affected by the depth of the hole. Therefore, the constant doping along the trench cannot cause Raman peak variation along the trench.

Heating can soften (redshift) both E^1_{2g} and A_{1g} modes of MoS_2. The focused laser increases the temperature locally and causes shifting in peaks. Although the laser power is constant during the scan, the substrate heavily affects the absorbed heat by the MoS2. The thermal conduction path changes from the substrate to the air by suspending the crystal. So, the suspended crystal absorbs more heat than the supported part using the same laser power. The depth trench also affects the amount of heat the MoS_2 can take from the laser, as the reflection back from the bottom can amplify the temperature increase in suspended MoS_2. The reflection from the bottom of the trench is closely related to the depth of the hole. We attributed significant shifts (≈ 4 cm^{-1} for the A_{1g} and E^1_{2g}) to enhanced light absorption due to reflection back from the bottom of the hole/trenches and less efficient heat dissipation in the suspended region.

We scanned the MoS_2 flake with lower laser power (100 μW) to avoid damaging the MoS2 by excess laser heating. Raman shift maps depicted in Figure 3.8c and d show softening of both characteristic Raman modes of MoS_2 on the suspended region. The shift amount is less than the device shown in Figure 3.6 due to lower laser power and different hole depths. Then, the 532 nm laser was parked over the suspended and supported region. Raman spectra were obtained at various laser power, and the Lorentzian function was used to extract the peak centers, shown in Figure 3.8c. As the laser power increases both E^1_{2g} and A_{1g} Raman modes soften linearly. Increasing temperature by heating the substrate or laser heating can soften

phonon modes. By heating the crystal, the lattice expands, and the equilibrium position of the atom and interatomic forces change, which affect the phonon energies and induce redshift in Raman modes. When the laser is pointed on the trench, E^1_{2g} and A_{1g} Raman mode peak shifts at different laser powers are obtained and depicted in Figure 3.8c. On the suspended part of the crystal, the slope of linear fitted lines is -3.2 and -3.8 cm^{-1}/mW for the A_{1g} and E^1_{2g} peaks, respectively. The Raman spectra were obtained in an ambient condition in which the convective heat loss mechanism by air is active [31][32][33]. The slightly different values reported in other studies can be related to different thicknesses of MoS_2, hole geometry, depth and measuring under vacuum or ambient conditions. Vacuum conditions can effectively suppress the air's heat dissipation, resulting in higher local temperature and, subsequently, higher redshifts. Thin layers of MoS_2 are relatively transparent, and reflection from the trench bottom amplifies the Raman signal by increasing the absorption. Therefore, the thickness of the MoS_2 flake and the hole depth also affect the heating process and results in different Raman slope change values.
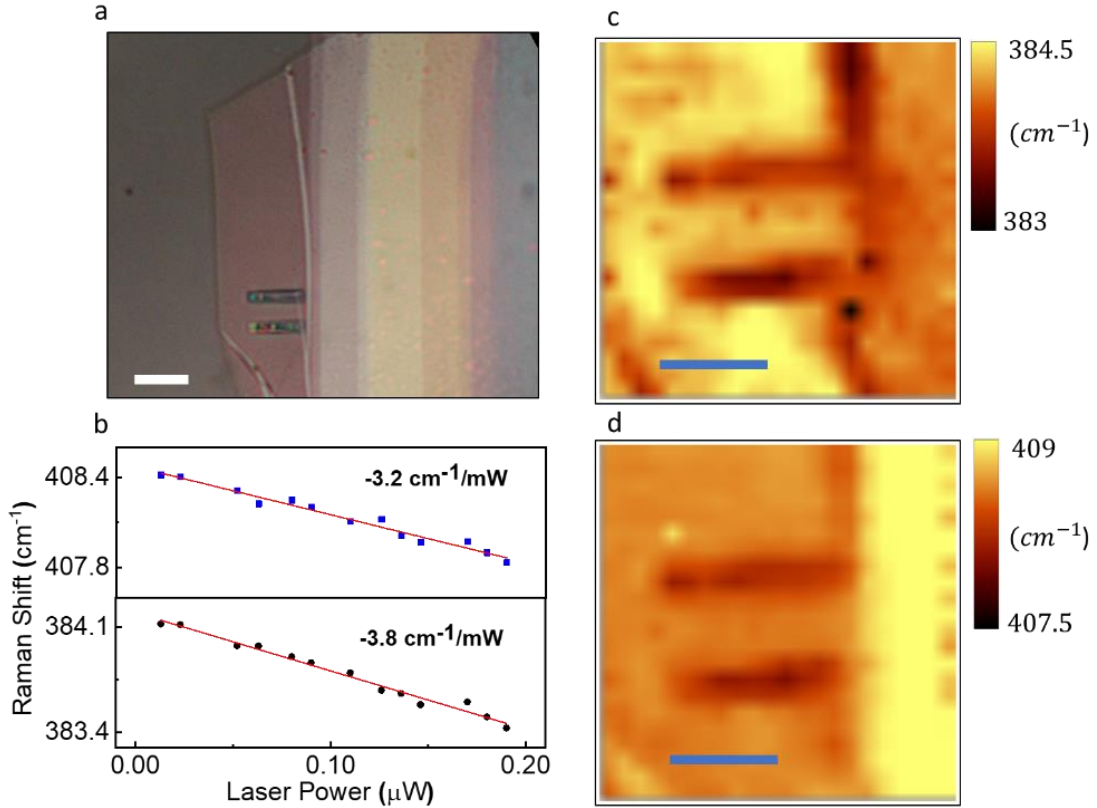
Figure 3.8: 4 (a) Optical image of transferred MoS_2 on the staircase trench structure. (b) Raman shifts vs. laser power on the suspended region of MoS_2. Raman peaks exhibit redshift due to increased temperature by higher laser power. (c) and (d) Raman intensity map of the E^1_{2g} and A_{1g} mode, showing that hating by laser is more effective on the suspended regions. The scale bars are 4 μm.

3.5   Wrinkles formation on suspended region

After transferring the MoS_2 crystals, we observed spontaneous wavy patterns (Ripples) formation on the suspended region of some samples with trench structure. The optical image of the transferred MoS_2 crystal is shown in Figure 3.9. The crystal bend and sticks to the bottom of the lowest trench, as seen from the line height trace in Figure 3.9c. The MoS_2 is suspended on the other trenches, and the bulge height is around 15nm. Then we focused on the wavy pattern forming on suspended MoS_2. The zoomed AFM and KPFM scan maps are shown in Figure 3.9d and e. Our observation shows that the ripples are not necessarily formed in all suspended

crystals. We should note that 2D materials can create ripples with out-of-plane deformation less than 1nm, reported in literature using high-resolution transmission electron microscopy (HRTEM) and high-resolution AFM [34][35]. The ripples are mainly perpendicular to the edge of the trench and have nearly periodic patterns with slightly different wavelengths. Using the sinusoidal function, the out-of-plane displacement Z of the ripples can be obtained as

$$Z = A \sin(2\pi y/\lambda)$$

Where A, λ are the maximum height and wavelength of the ripples. For the ripple shown in Figure 3.9d we found the A and λ values around 15 nm and 2.5 μm, respectively. We observed small variations in the workfunction of the ripple structures, which can originate from the formation of varying stress regions. The deformation by ripples induces inhomogeneous charge distribution and surface potential [36]. The difference between the valley and the peak is about 8 ev which is much lower than the difference between supported and suspended parts, as seen in the workfuncion map in Figure 3.9e.

The stress applied to MoS2 while transferring or/and heating the sample to 160 °C (during making indium contacts) can form and alter these ripple structures' morphology. The ripple morphology, wavelength, height and orientation can be controlled by applying strain. Annealing the samples changes the morphology of these patterns as the thermal expansion coefficient of substrate and MoS_2 are different [37].
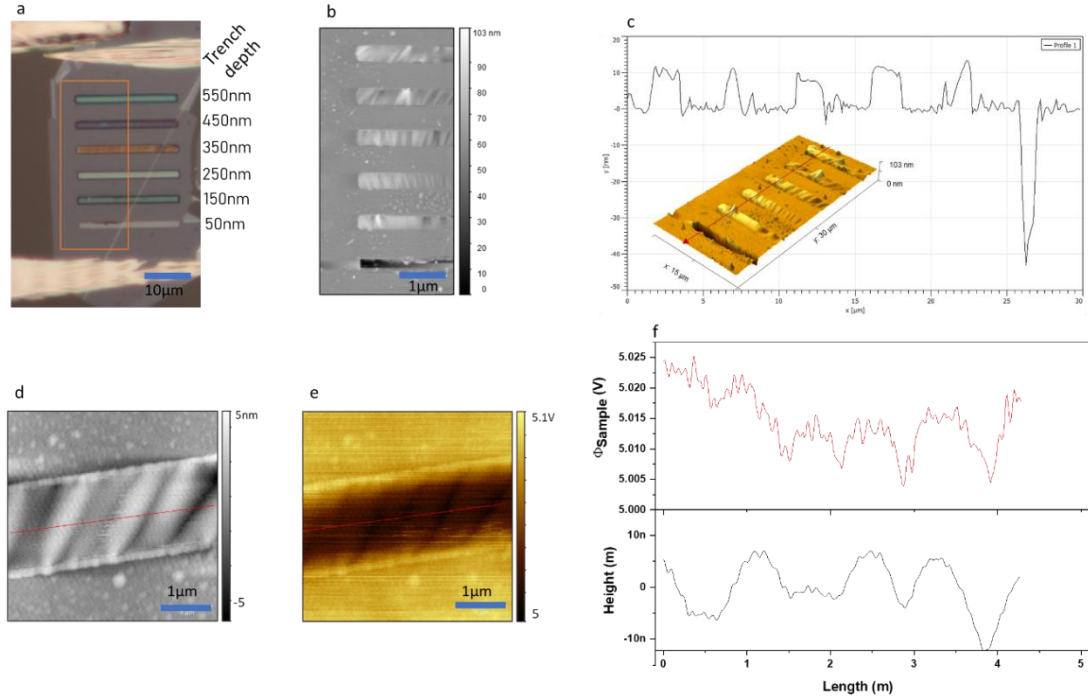
Figure 3.9: (a) Optical image of transferred MoS$_2$ on trenches with different depths. (b) AFM height trace map. (c) line height trace along the red arrow shows MoS$_2$ bulges up 12 nm on the suspended regions. (d) Zoomed AFM maps showing ripples on the suspended region. (e) workfunction mapping on the suspended region. (f) the height and workfunction variation along the red line in previous panels.

3.6 Photocurrent generation at thermoelectric Junctions

To study the effect of substrate on the photocurrent response of MoS$_2$, the thin crystals transferred on the various substrate with holes/trenches. The substrate heavily influences the atomically thin 2-dimensional material properties. Separation from the substrate creates a junction in a single flake of MoS$_2$ with different doping characteristics. Figure 3.10a shows the optical image of two devices fabricated on one MoS$_2$ crystal. The reflection intensity and photocurrent maps of the region marked by the green box are depicted in Figure 3.10 d and e. The photocurrent map exhibits a bipolar response at the boundaries of the supported and suspended parts. No photocurrent is generated at the center of the suspended part, and the

51

maximum photocurrent is generated at the junctions of supported and suspended regions. The bipolar response is consistent with the photothermoelectric effects. The current is derived by the potential difference when the junction of two materials with different Seebeck coefficients is heated.

The height trace map of the device obtained by AFM is shown in Figure 3.10c. The thickness of the crystal along profile 1 was measured as 4 nm. The depth of the trenches measured with AFM was 120 nm. The crystal can bend, stick to the bottom and walls, or be suspended. The suspended region of MoS_2 makes a big difference in optical contrast, photocurrent generation, and Raman spectra. The color contrast pointed by the green arrow in the optical microscope image implies that the crystal is suspended on the trench. This optical observation is confirmed by height trace mapping and SEM images. The crystal bulged up 20 nm. MoS_2 crustal bent inside and stuck to the substrate on the other trench. The suspended part generates ten times stronger photocurrent than the supported part in both devices.
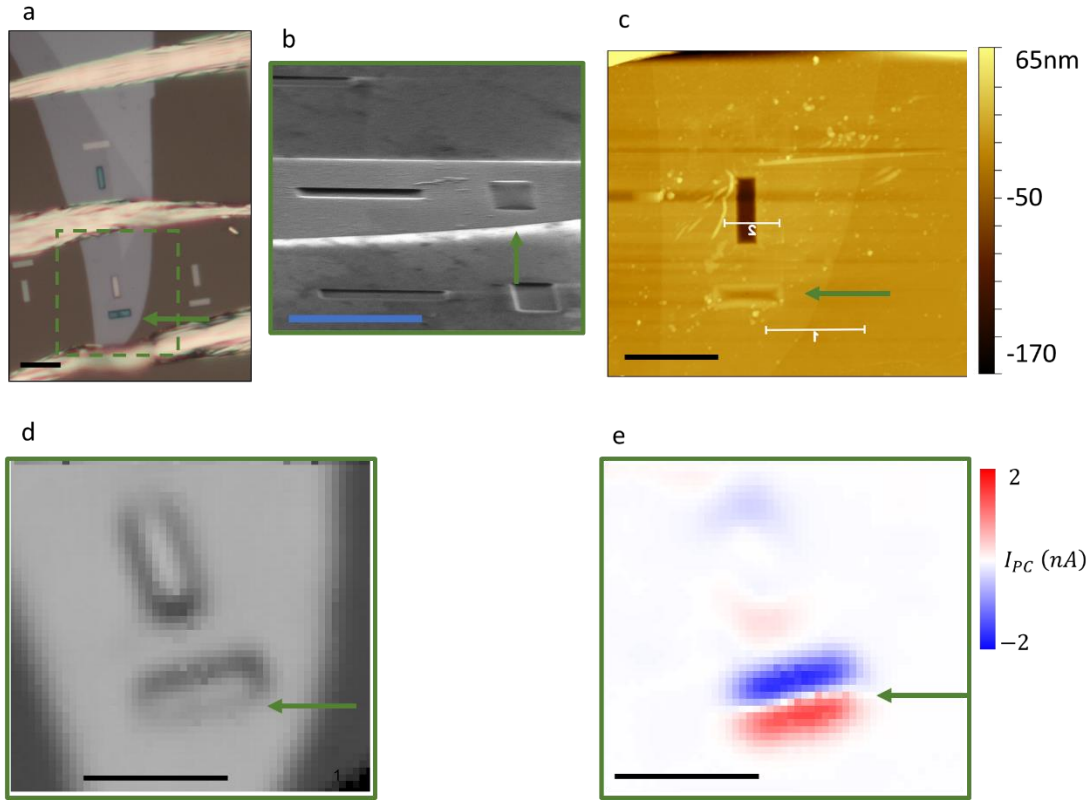
Figure 3.10: (a) Optical image of MoS$_2$ Devices with perpendicular trenches (b) SEM images of crystal. The MoS$_2$ is suspended on the right trench, pointed by green arrow. (c) AFM height trace map. Crystal thickness is 4 nm obtained from the height trace along profile 1. MoS$_2$ bent 120 nm inside the trench, along profile 2. (d) The reflected intensity map using 40μW, 532 nm laser (e) SPCM maps obtained under 0 bias voltage show a strong bipolar signal from the junction of the lower trench where the crystal is suspended. Scale bars are 5μm.

The device marked by red dashed rectangle in Figure 3.11a shows a similar thermoelectric effect on the suspended trench. By tilting the stage of SEM up to 70°, it becomes obvious that one hole is stuck to the substrate while the other one is bulged up (Figure 3.11b and c). We pointed the suspended part by the red arrow. At the side of suspended regions, strong photocurrent is generated (Figure 3.11f). Suspending the crystal eliminates the effective thermal conductive path from the substrate. So, we can expect the laser causes a higher local temperature on the suspended part compared to the supported part. We can verify this hypothesis with

Raman spectroscopy, as the prominent peaks of MoS_2 are highly sensitive to temperature variation. As can be seen from the Raman map of out-of-plane A_{1g} shifting in Figure 3.11d, the MoS_2 on the suspended trench experience redshift by softening the Raman mode due to absorbed heat by the laser. The intensity of the characteristic peaks also increased at the suspended region (Figure 3.11e). The Raman observations indicate that the temperature rises at suspended part is more than at the supported part. So, illuminating the junction of the supported and suspended parts results in a considerable temperature gradient. The existence of a temperature gradient is a prerequisite for the thermoelectric effect. This high temperature gradient at the junction can explain the stronger photocurrent generation from the junction of supported and suspended region.

The substrate heavily affects the Seebeck coefficient as the parameters like phonon mean free path, electron density, doping, and interfacial Coulomb impurities alter in the presence of the substrate. Because of the difference in the Seebeck coefficient, a thermoelectric junction, or thermocouple, is formed at the junction of supported and suspended parts. The photothermoelectric electromotive force can be generated by heating this junction with focused laser light.
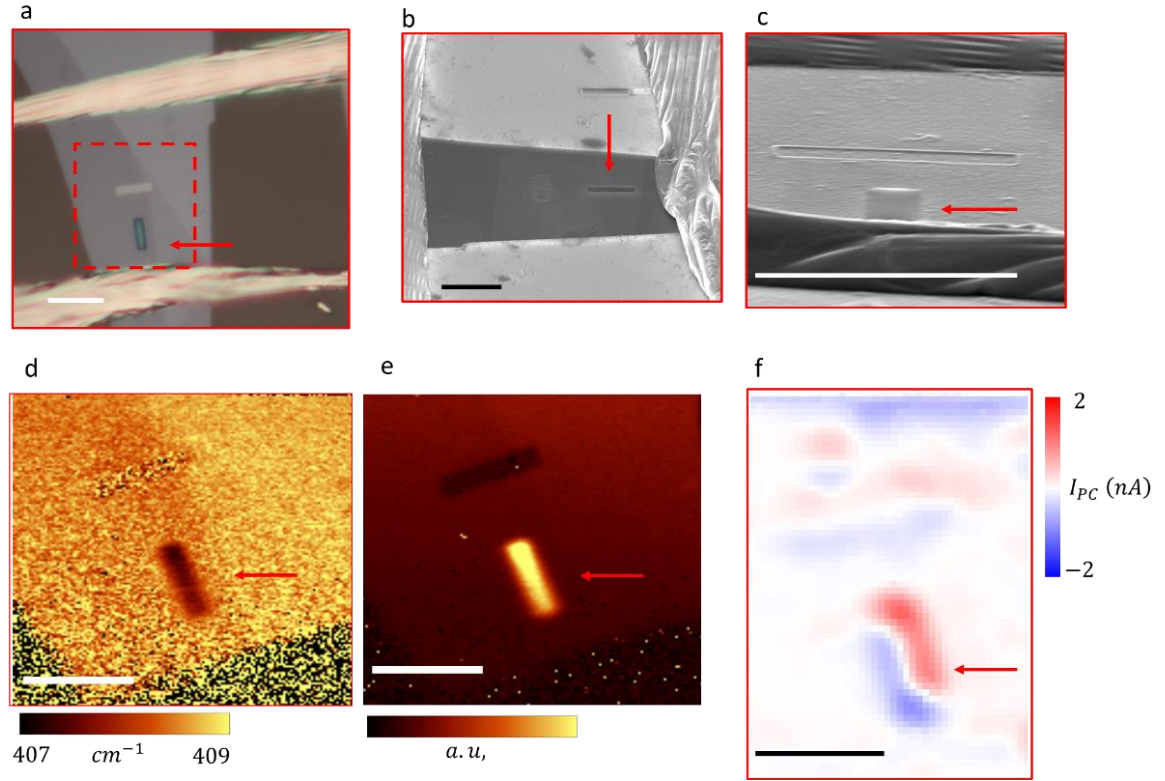
Figure 3.11: (a) Optical image of MoS_2 Devices with perpendicular trenches (b) and (c) SEM images of crystal. The MoS_2 is suspended on the trench pointed by the red arrow. (c) AFM height trace map. Crystal thickness is 4 nm obtained from the height trace along profile 1. MoS2 bent 120 nm inside the trench, along profile 2. (d) and (e) Raman shift and intensity map of the A_{1g} mode. The crystal is suspended in the trench marked by the red arrow. So the temperature rise is higher than the other hole, causing redshift and enhanced intensity in the suspended region. (f) SPCM maps obtained using 40µW, 532 nm laser, under 0 bias voltage, show a bipolar response from the suspended crystal on the trench marked by the red arrow. Scale bars are 5µm.

3.7   Kelvin probe force microscopy

In the following, the effect of substrate on the topography and surface potential of MoS_2 is studied by performing Kelvin probe force microscopy (KPFM). The substrate can modulate the type and number of charge carriers by donating charges. Also, the trapped charges at the interface of the MoS_2 and substrate can gate the MoS_2 locally. The variations in the electrostatic properties lead to

modulation of the MoS$_2$ workfunction. KPFM can detect small changes in the Surface potential difference (SPD) with nanometers special resolution. Density functional theory (DFT) study of MoS$_2$ showed that even small changes in chemical potential can modulate the Seebeck coefficient[38]. These theoretical studies are also supported by gating experiments in which the Seebeck coefficient can be modified by changing the chemical potential and carrier concentration. In our devices, suspending the crystal modifies the chemical potential and Seebeck coefficient, leading to the formation of the thermoelectric junction.

Isolating the crystal from the substrate eliminates the trapped charges at the interface and charge donation by the substrate. Therefore, KPFM is capable of accurately measuring of band bending of MoS$_2$ on supported and suspended parts. This device contains a staircase trench structure (Figure 3.6) studied using KPFM. Figure 3.12 shows the height trace map, uncalibrated SPD maps and SPCM map of the device. As seen from the graph in Figure 3.12c, the supported and suspended parts of the crystal have 50 mV difference in surface potential, which is consistent with the reported SPD value for suspended-supported MoS$_2$. The MoS$_2$ is naturally n-doped semiconductor. Only in specific device structures and high negative gate voltages, holes can become major charge carriers [39][40]. To reverse the charge carriers from electrons to the holes, the SPD around 500 mV is reported [41], an order of magnitude higher than the SPD we measured from the junction region. The slight change we measured in Fermi Level (50mV) cannot make a suspended MoS$_2$ a p-type semiconductor. On both sides of the junction, the supported and suspended region, the same type of charge carriers (electrons) would be prevalent. The n-n junction formed between the supported and suspended parts cannot create the strong built-in electric field needed to separate photoinduced charge carriers [42].

The reflection and SPCM maps taken with 406 nm laser at 50 μW are shown Figure 3.12 d and e. In the first trench, the SPD reaches 150mV for the crystal stuck to the hole. However, the photocurrent from trench 1 is less than others. Since the crystal above the left trench stuck to the bottom, heating by the laser is

suppressed due to the conductive path of the substrate at the bottom of trench 1. The strong photocurrent generated from the trenches that MoS_2 is suspended. The photocurrent is changing along the suspended region due to variations in absorbed laser power. This observation implies the thermoelectric origin of the observed signal of the SPCM map.
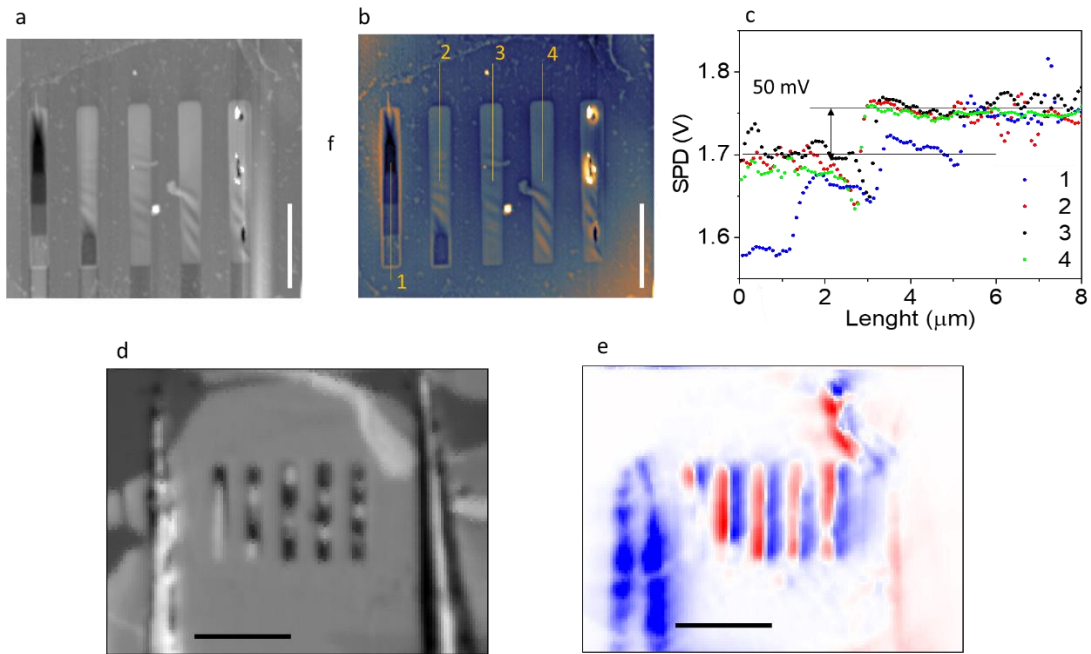
Figure 3.12 (a) AFM height trace map of MoS_2 on the staircase trenches (b) KPFM map shows the variation SPD. (c) The line traces are taken along the lines previous panel. Suspended crystal shows 50 mV difference in SPD. (d) The reflected intensity map using 50μW, 406 nm laser. (e) SPCM maps obtained under 0 bias voltage. The sides of trenches generate strong photocurrent where the crystal is suspended. The crystal sticks to the bottom of the left trench, and photocurrent generation is suppressed. Scale bars are 10μm.

3.8 Scanning thermal microscopy (SThM)

Scanning thermal microscopy (SThM) is performed to investigate the local thermoelectric properties of the junction with nm spatial resolution. The schematic of the measurement is shown in Figure 3.13a. SThM is an AFM based measurement. The tip temperature increases by a resistor in the cantilever. Then the hot tip scans the surface while the thermoelectric voltage is recorded from metallic contacts, which gives a thermovoltage map of the surface. This method uses a hot AFM tip as a heating source, so photovoltaic effects are excluded in the absence of light illumination to the sample. Figure 3.13 shows the optical image of the device and a zoomed view of the rectangle holes. The STHM maps in Figure 3.13f shows the same bipolar response from the junction of supported and suspended regions. This observation verifies that the photocurrent signal (Figure 3.13g) has a thermoelectric origin. A thermovoltage is developed when the hot AFM tip heats a junction area with two different coefficients. Similarly, a photocurrent is generated when the laser is heating the junction area.
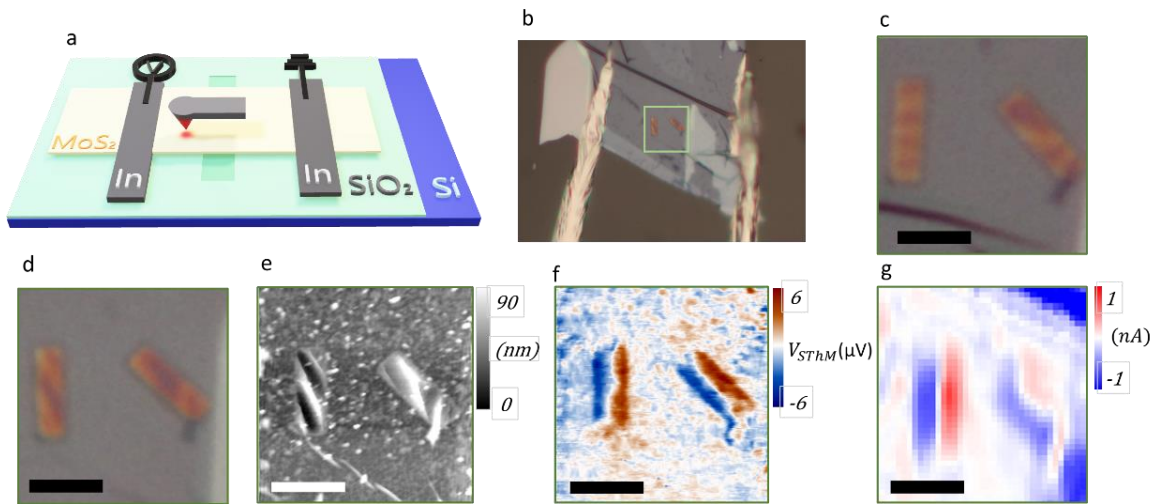
Figure 3.13: (a) The schematic of the SThM method. A hot AFM increases the temperature of the MoS_2 locally while scanning the surface. The thermovoltages measured from each point are combined to make a map. (b) The optical images of the device. (c) Zoomed optical image from the trench area after transferring the crystal. Interestingly, wrinkles are distinguishable in optical images. (d) The wrinkles orientation changed when the samples heated up to 170 ℃ to make indium contact. (e) AFM height trace map showing that MoS_2 is suspended on the trenches.

(f) SThGM thermovoltage map (g) SPCM map of the same region. Both thermovoltage and photocurrent maps show a similar bipolar response from the supported-suspended junction. Scle bars are 3µm.

3.9   Gating measurements

The field-effect transistor (FET) is constructed by transferring the thin layer of MoS$_2$ on the degenerately doped silicon substrate with a SiO$_2$ layer as a dielectric. Silicon (Si) back-gate is used to modulate the charge carrier density of MoS$_2$ channel.

Before discussing the gating experiment results, the damages during gate dependence measurement in the suspended part of MoS$_2$ will be reported. The MoS$_2$ flakes are transferred on Si wafers coated with 1µm of SiO$_2$ coating. Figure 3.14 shows the gradual degradation of the crystal, which starts from the suspended part and spreads to the supported region. This degradation spreads by applying more gate voltages to Si as a back-gate. Degradation of the MoS$_2$ crystal was confirmed by Raman spectroscopy. Raman doesn't show any MoS$_2$ peak from the damaged region, although the crystal was not removed from the damaged area. The photocurrent signal diminishes during gating by spreading damage into a junction area, making it impossible to study the thermoelectric response to gating. The device with a long trench with open ends also faced the same type of damage, so the trapped air within the hole may not be the reason behind the degradation. We should note that the thermal annealing at 300 ℃ in Argon atmosphere for 3 hours could not revive the device. The origin of such degradation is still unknown to us and has not been reported in the literature. Drilling holes with ions may cause some point defects in the dielectric SiO$_2$ layer. To resolve that, after drilling the trench, we covered the surface with another layer of Al$_2$O$_3$ dielectric.
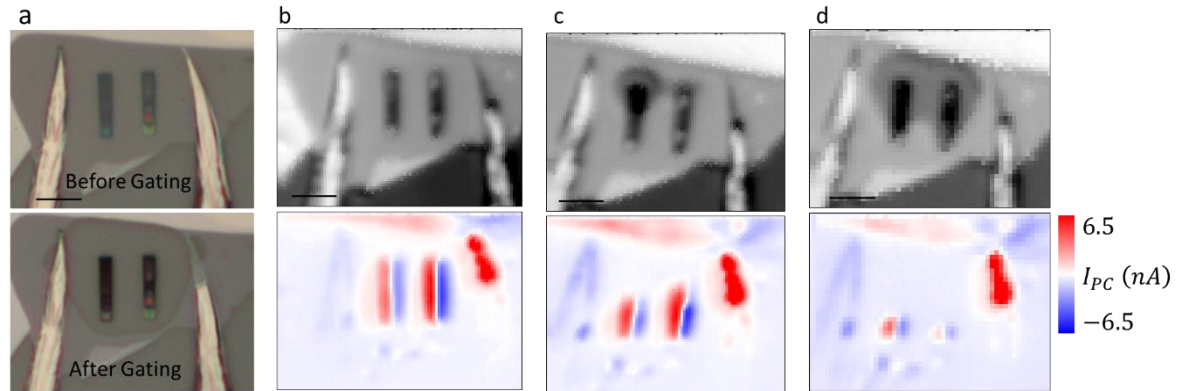
Figure 3.14: (a) optical images of the MoS$_2$ device before (upper panel) and after (lower panel) SPCM with applying gate voltages. (b) Reflected and SPCM map using 86μW, 532 nm of on sample without applying gate voltage. (c) and (d) Reflected and SPCM maps by applying V$_G$= -15V. The degradation started by applying gate voltage and progressed along the trenches. Scale bars are 5 μm.

The additional Al$_2$O$_3$ layer introduced after milling holes to avoid degradation during measurements. Using Atomic Layer Deposition, 30 nm Al$_2$O$_3$ is deposited on the surface, and then MoS$_2$ crystal is transferred on the coated substrate. The devices fabricated on the Al$_2$O$_3$ modified surface didn't show any degradation sign and were preserved during gating measurement. Figure 3.15 shows the schematic and the optical image of the device used for gating experiments.
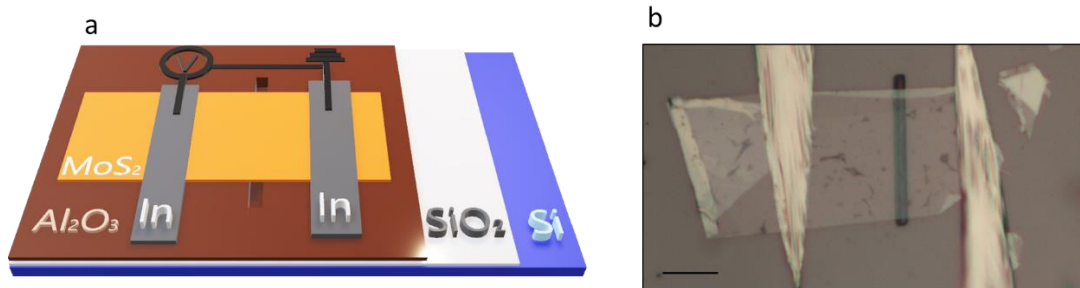
Figure 3.15: (a) schematic of the device in gating measurements. The gate voltage is applied to the Si substrate. The Al$_2$O$_3$ is coated to cover possible damages in SiO$_2$ layer near the trench area. MoS$_2$ crystal is transferred on the trench. (b) Optical microscope image of the MoS$_2$ device used in the gating experiment. The substrate is coated with 30 nm Al$_2$O$_e$ before transferring MoS$_2$. Scale bars are 10 μm.

The current passing through the device is measured while sweeping the voltage bias. Figure 3.16a and b show the IV curves at different biases under light illumination and dark state, respectively. In the voltage sweep range, the IV curves are linear, which indicates the ohmic behavior and the absence of Schottky contacts. As can be seen from Figure 3.16c, even at high negative gate voltages, no hole conduction was observed, which shows the typical behavior of n-type MoS_2 semiconductors. On the positive side of gate voltage, the number of dominant charge carriers (electrons) increases, and conductivity increases. Vice versa, on the negative side, the channel is depleting from the electrons, and the resistivity increases dramatically. We should note that drain current saturation was not observed at high positive gate voltages because of a thick layer of SiO_2, similar to other studies using SiO_2 as a back gate [43]. The current difference between the dark current (I_{Dark}) and under illumination (I_{Light}) current determines the photocurrent, $I_{PC} = I_{Light} - I_{Dark}$. Photoconductive effect is the origin of the measured photocurrent at global light illumination under applied bias.
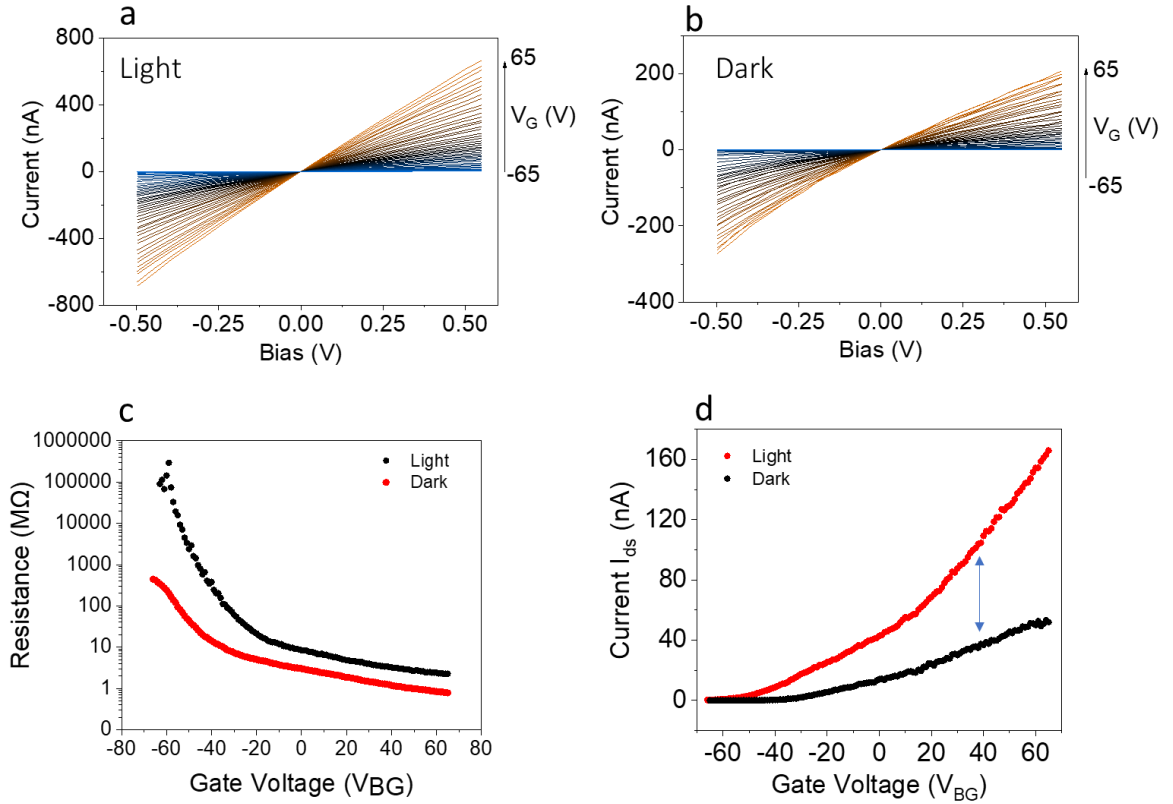
Figure 3.16: (a) The current vs. voltage graph in the range of -65 to 65 V back-gate voltage under white light illumination. (b) Current vs. back-gate voltages in the range of -65 to 65 V back-gate voltage under dark condition. (c) The resistance under light and dark condition. (d) current vs. back-gate voltages with 0.15 mV bias. (d) the difference between current passing through device is photocurrent generated by the photoconductive effect.

As mentioned, the Seebeck coefficient can be modified by controlling the density and type of charge carriers, which is demonstrated in many theoretical and experimental studies. Gating MoS$_2$ in transistor device structure enables us the control the charge carrier type and density [44]. The Seebeck coefficient is gate-dependent and modeled using the Mott relation [45]:

$$S = \frac{\pi^2 k_B^2 T}{3e} \frac{1}{R} \frac{dR}{dV_g} \frac{dV_g}{dE}\bigg|_{E=E_F}$$

In the equation, k_B is the Boltzman constant, T is temperature, E_f is fermi energy and V_g is the voltage applied to the gate. Electrons are mostly considered dominant charge carriers in MoS_2, although there are few researches in which holes become dominant charge carriers by applying enough high negative gate voltages [46][40]. If charge carriers polarity reverses from negative to positive, the derivative of resistance $(\frac{dR}{dV_g})$ will be change. So, the sign of Seebeck coefficient can change from negative for n-doped MoS_2 to positive for p-doped MoS_2 and the thermoelectric response disapears as the Seebeck coefficient reaches around zero. Also, based on the equation, the Seebeck coefficient is expected to approach zero for highly electron doped MoS_2 at high positive gate voltages due to resistance saturation in high doping level ($\frac{dR}{dV_g} \approx 0$).

The MoS_2 crystal transferred on the Al_2O_3 surface coated substrate with the trench. The optical image, reflection maps and photocurrent maps are shown in Figure 3.17. It can be seen from photocurrent maps that increasing the gating voltage to positive values reduces the thermoelectric response, which agrees with our prediction and other previous studies [44] [47]. Figure 3.17c illustrates the signal collected from the maps along the dashed arrow in Figure 3.17b. Each line was collected at different gate voltages with 20 V steps. It shows that by depleting the charge carriers in high negative gate voltages, the thermoelectric response is enhanced.
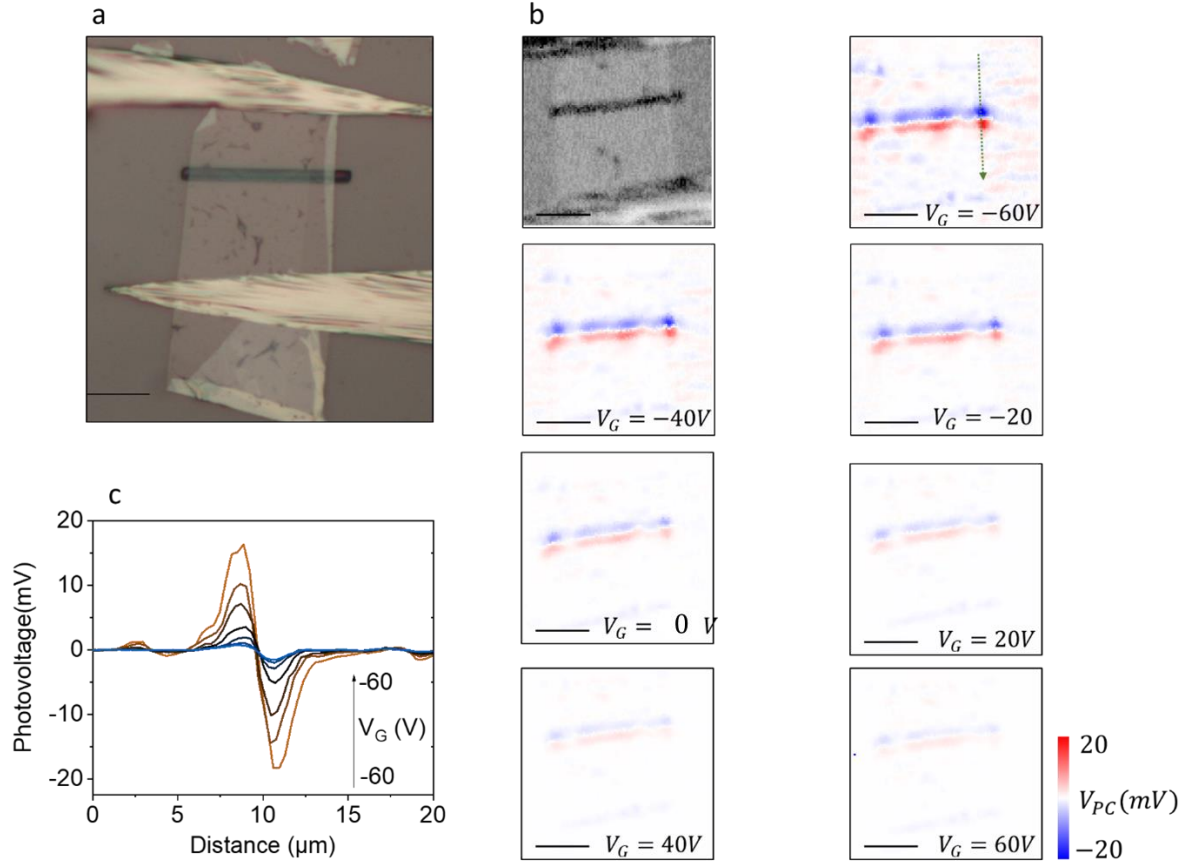
Figure 3.17: (a) optical image of the device. (b) the reflection map and photovoltage maps collected without chopper and Lock-in amplifier (c) photovoltage line trace along the green dashed arrow in previous panel. Negative gate voltages enhance the photovoltage as charge carriers are depleted from the channel. The scale bar is 10 µm.

Then, we parked the laser on points near and far from the junction (pointed by the green arrow in Figure 3.18), and the photovoltage signal was measured while sweeping the gate voltage from negative to positive. The photovoltage graph is shown in Figure 3.18a. The signal increases negative gate voltages, but we did not observe the peak or photovoltage sign inversion. As discussed before, the Seebeck sign change is expected when the hole becomes the dominant charge carrier. The resistance vs. gate voltage graph (Figure 3.16c) does not show any reduction in resistance even at high negative gate voltages. This indicates that MoS_2 on SiO_2 is

a typical n-dope semiconductor without any measurable hole conductance. Therefore, the Seebeck coefficient sign and the photovoltage direction remained the same.
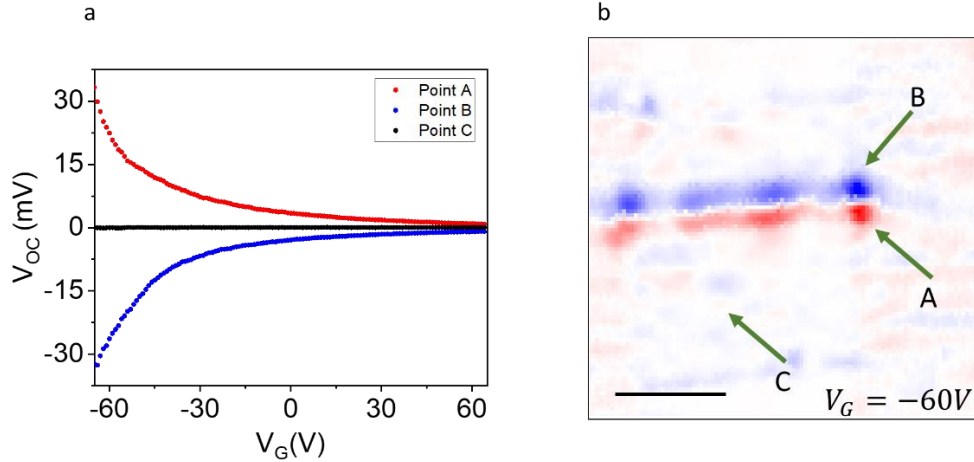
Figure 3.18: Photovoltage data collected from points A, B and C. The photovoltage sign did not change even at high negative gate voltages. No Seebeck coefficient sign inversion is observed due to of lack of hole conduction.

We should note the importance of substrate in determining the charge carrier concertation and type. Many chemical and physical contaminants like water molecule and other ambient impurities can be absorbed into the surface of SiO_2. In addition, SiO_2 Surface is not flat and has roughness on the surface. The high density of traps is forming on its surface because of dangling bonds and impurity molecules on the surface. The electron and hole can occupy these trap states when the crystal is transferred on the SiO_2. For example, both n-dope and p-dope graphene have been previously observed on SiO_2 surfaces, depending on different surface polarities [48]. The charge carrier characteristic of the thin layer of MoS_2 is also very sensitive to the substrate. For instance, the polarity of charge carriers is changed from electron to hole by transferring MoS_2 from the SiO_2 to the polytetrafluoroethylene (PTFE) substrate. Ambipolar MoS_2 transistors, in which electrons are dominant in positive gate voltages and holes are the majority charge carrier in negative gate

voltages, are made by using hBN and polymethyl methacrylate (PMMA) as a substrate [40][46].

In our devices, the SiO_2 dielectric layer suppresses the hole conduction on the supported regions. The trapped charge at the surface of SiO_2 causes Fermi level pinning (FLP) at the interface of MoS_2 and SiO_2. Although the suspended part is isolated from the substrate, the electric field imposed by the gate might not be enough to alter the charge carrier type. No Seebeck coefficient sign inversion (negative to positive) was observed as the hole conduction is limited in MoS_2 on the supported and suspended region. The previous report showed a typical n-type behavior for a suspended single-layer MoS2 devices [49].

We investigate the photoresponse of hBN-supported MoS_2 to emulate the suspended region on the hole. hBN is commonly used to improve the performance of MoS_2 transistors because of its hydrophobic, smooth and atomically flat surface. The hBN layer limits unintentional doping by screening the charge trap states.

Figure 3.19a shows the hBN and MoS_2 heterostructure in which MoS_2 crystal is suspended on the trench. First, a hBN crystal was transferred on the substrate, then MoS_2 crystal was placed on hBN and trench. Using this configuration, we eliminated the effect of MoS_2 thickness, as the number of layers affects Raman characteristic peaks and the workfunction of MoS_2. Figure 3.19c and d show Raman map shifting and intensity of A_{1g} (408 cm^{-1}). In the suspended region, the Raman peak exhibits red-shift, and the its intensity increases. On the contrary, the supported region by hBN shows a blueshift and reduced intensity. Another prominent peak of MoS_2, E^1_{2g}, also showed the same trend. As the thermal conductivity of the MoS_2 is relatively low, Once the MoS_2 is isolated from the substrate, the temperature increase can be relatively high, leading to lattice expansion and redshift in the Raman peak. The temperature rise to 85 ℃ is estimated when the 100 μW laser illuminates the suspended region [33]. Although, when MoS_2 is in contact with the substrate, the heat can dissipate from the vast interface by the substrate. By replacing SiO_2 with hBN, the heat dissipation is greatly amplified. In addition, hBN provides a clean and flat surface for MoS_2 that

screen the charge impurities of the SiO_2 substrate. Interestingly, the cooling effect of the hBN was still effective when both hBN and MoS_2 are suspended on the trench. Recently, high interfacial thermal conductance between hBN and MoS_2 has been reported [50]. This effective conductive path can suppress the temperature increase by the laser, causing the blue shift, and reduce the intensity of the MoS_2 Raman peaks.
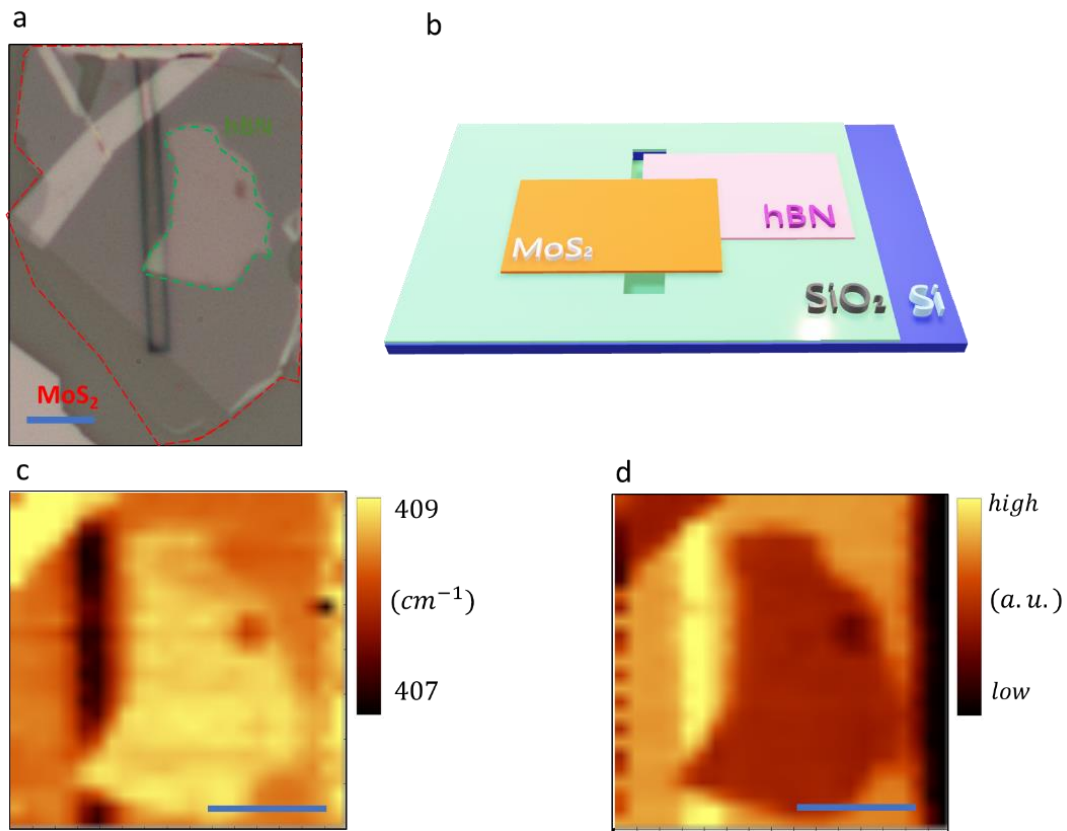
Figure 3.19 (a) Optical image of MoS_2 device suspended on the hole and partially supported by the hBN (b) the schematic of the heterostructure in which MoS_2 placed on top of hBN and trench and (c) and (d) Raman shift and intensity map of the A_{1g} mode. Heat dissipation is more effective when MoS_2 is in contact with hBN. Also, placing MoS_2 on the atomically flat surface of the hBN stiffens the bonds, resulting in blueshift of Raman peak of MoS_2. The Raman peak exhibits redshift on the suspended region due to temeperature rise. Scale bars are 5μm.

The height trace and SPD map of the same device is obtained from the white dashed rectangle region shown in Figure 3.20a. hBN thickness measured by AFM is around 10 nm. The line trace map shows 58 and 35 mV increases in SPD on hBN and trench, respectively. The MoS_2 crystal on both hBN and trench shows a similar increasing trend in SPD. The rise in SPD can be explained by reduced interfacial doping as the hBN layer can screen the trapped charge of the substrate. By suspending the MoS_2, the substrate effect is eliminated, although the crystal surface is not as flat as the MoS_2 on the hBN. The shift in SPD at the SiO_2 and hBN-supported MoS2 can be used to make a thermoelectric junction, which will be discussed in the following.
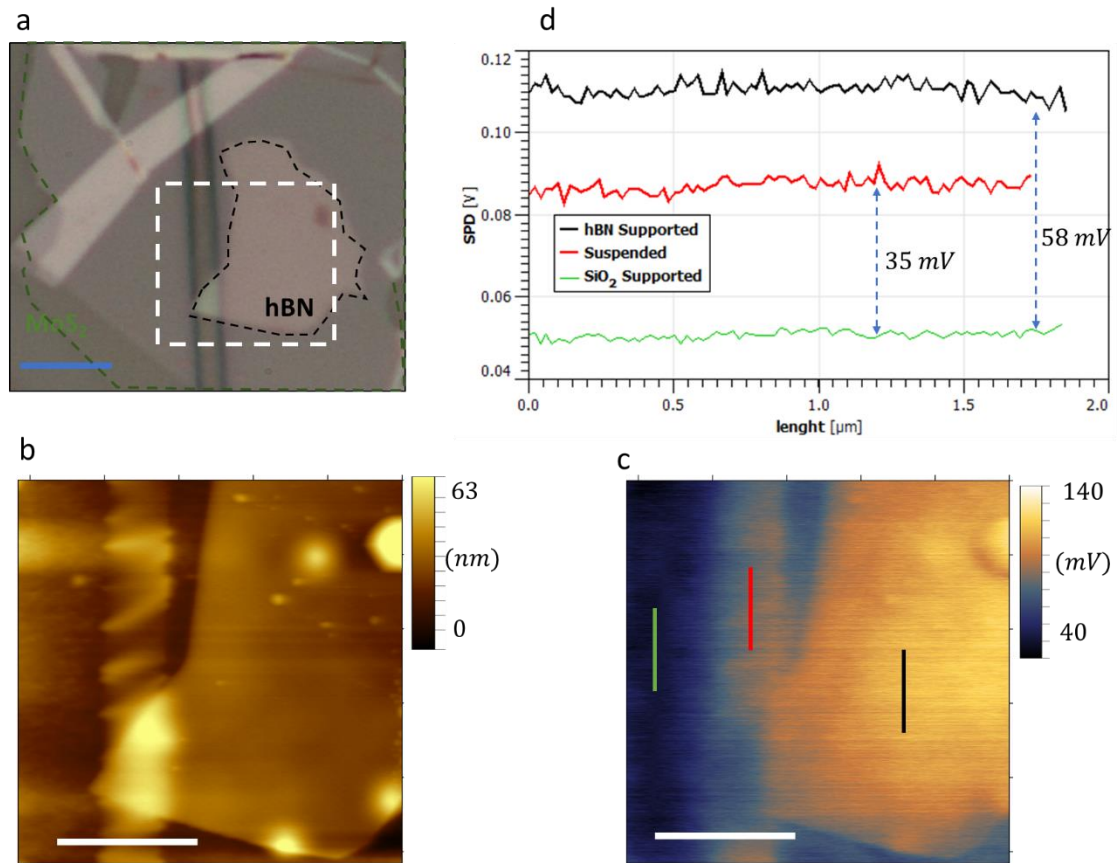
Figure 3.20 (a) Optical image of MoS2 device suspended on the hole and partially supported by the hBN (b) AFM height trace map (c) KPFM map shows the variation SPD. (d) SPD line trace from the SiO_2-supported, suspended and hBN-supported MoS_2. Reduced interfacial doping by suspending the crystal and supporting with hBN resulted in SPD variation. Scale bars are 2 μm.

68

The optical graph of the partially hBN-supported device is shown in Figure 3.21a. As can be seen from the optical graph, the MoS_2 flake thickness is not uniform. The number of layers is obtained using AFM. Considering each layer of MoS_2 is about 0.65 nm, the thickest, middle and thinnest parts of MoS2 consists of 11, 9 and 6 layers, respectively. Some bubbles form mainly after heating the crystal up to 165 ℃ while placing indium contacts. The diameter and height of the biggest one pointed by the green arrow are around **2μm** and 90 nm, respectively. By placing layer material on top of each other, the van der Wals forces between layers squeeze the contaminations like water and hydrocarbon into the bubble cites. So, the self-cleaning process on the flat areas is done by gathering the contamination and forming bubbles [51]. Raman mapping of E^1_{2g} peak shows a slight blue shift and reduced intensity of the hBN-supported MoS_2 compared to the SiO_2-supported MoS_2 region. As stated before, the stiffening of the Raman modes of MoS_2 in the hBN-supported region is related to fewer impurities and efficient heat dissipation by the hBN.
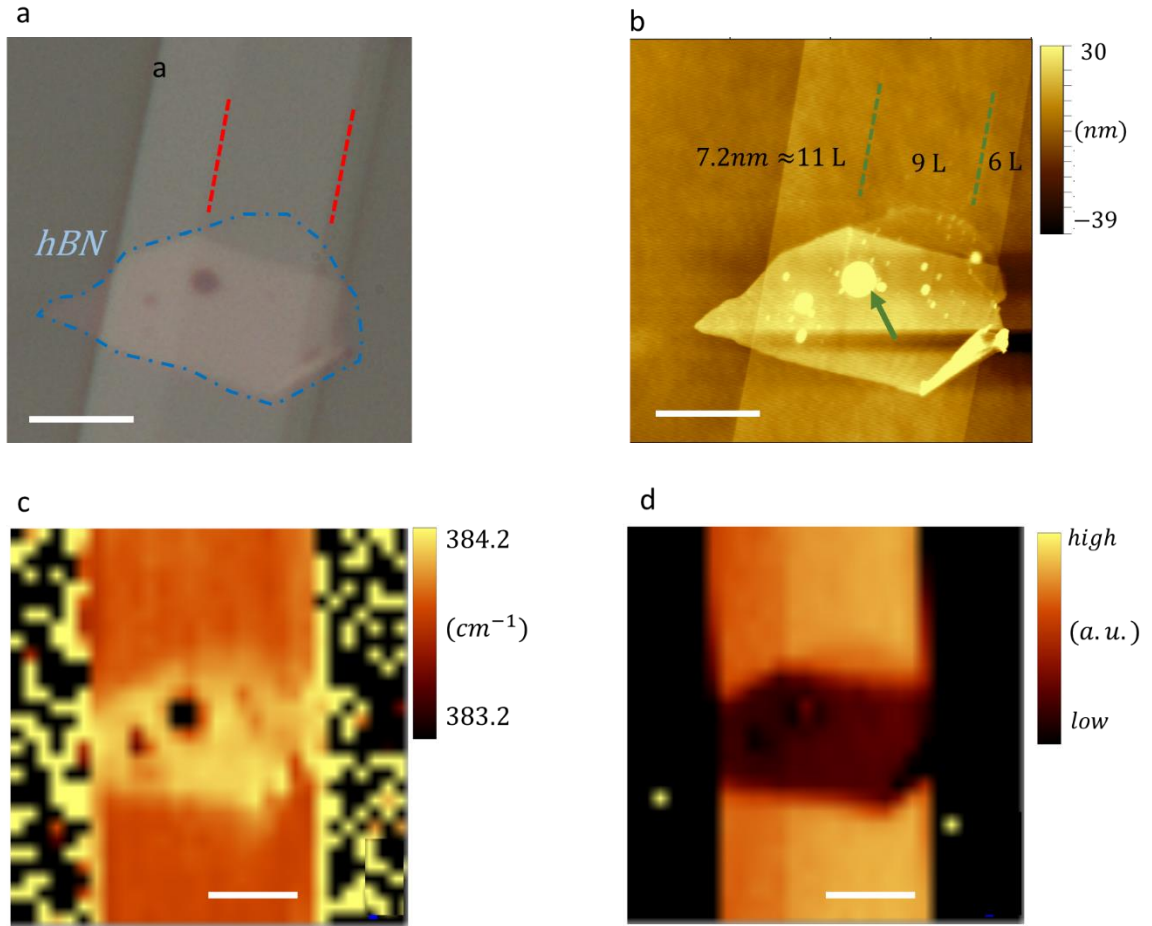
Figure 3.21 (a) Optical image of MoS$_2$ crystal partially supported by the hBN (b) AFM height trace map showing that thickness is not uniform. (c) and (d) Raman shift and intensity map of the A$^1_{2g}$ mode. Blueshift was observed on the hBN-supported region due to the stiffening of the bands and efficient heat conduction by the hBN. The bubble shows an interestingly high redshift, probably due to the high contamination concentration inside the bubble. Scale bars are 5μm.

Then we placed indium needles as metallic contacts and fabricated a back-gated transistor, as shown in Figure 3.22a and b. The IV curve at different gate voltages is obtained and depicted in Figure 3.22c. The overall device response to the gate voltage is a typical response of n-type semiconductor. By applying large negative gate voltages, the semiconductor channel is depleting from the charge carriers, resulting in increased resistance (Figure 3.22d). The previous report shows that

hBN layer as a substrate can develop hole conductance and ambipolar behavior in MoS$_2$ [40]. hBN layer covers a small portion of the channel length in the device we studied, which is not enough to promote hole conductance through the entire channel length.
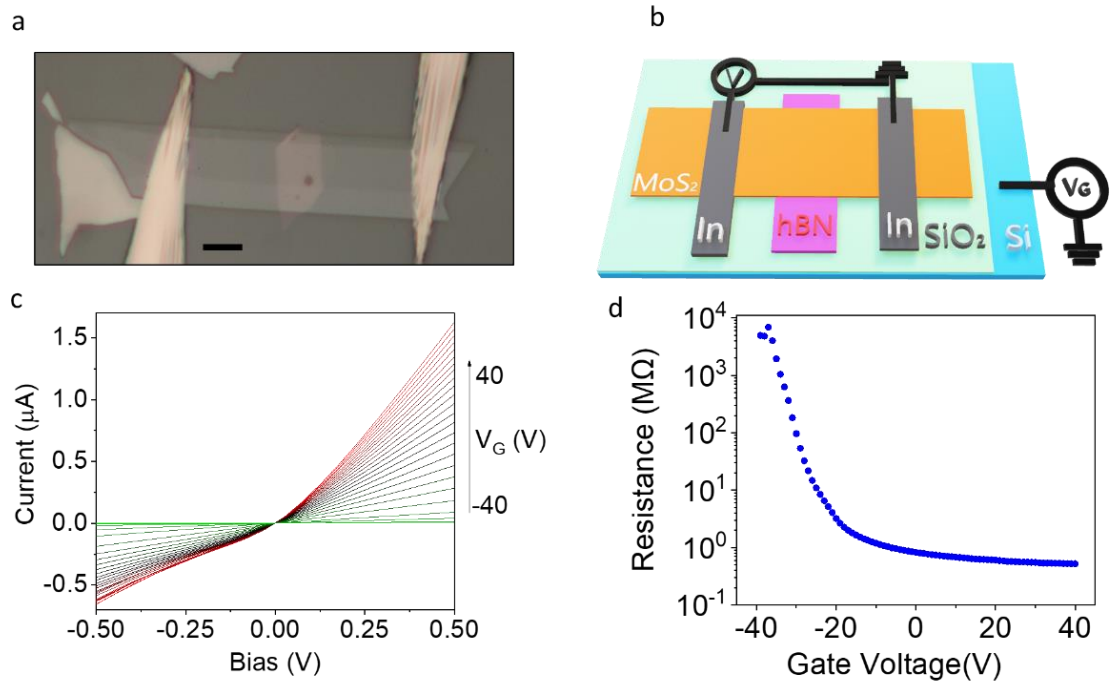
Figure 3.22 (a) Optical microscope image of the MoS$_2$ transferred on top of hBN flake. (b) schematic of the device in gating measurements. MoS$_2$ is partially supported by hBN. The gate voltage is applied to the silicon substrate. (c) The current vs. voltage graph in the range of -40 to 40 V back-gate voltage under white light illumination. (d) The resistance vs. gate voltage under white light illumination. Although hBN can promote hole conduction, no hole conduction is observed at negative voltages as the hBN-supported area is smaller than the channel length. The scale bar is 5μm.

A thermoelectric junction is formed at the junction of hBN-supported parts and SiO$_2$-supported parts. As can be seen from the reflection and photocurrent maps in Figure 3.23b a bipolar response comes from the junction between SiO$_2$ and hBN-supported MoS$_2$. Then, we studied the gate dependency of the photocurrent

on different positions. The photocurrent is measured while sweeping the gate voltages from positive to negative, as shown in Figure 3.23c and d. The photocurrent generated on the junction of SiO_2 and hBN-supported part decreases by applying positive gate voltages. Reducing photocurrent by increasing carrier concentration on the positive gate voltage is similar to the MoS_2 on the trench devices. On the other hand, applying a negative gate voltage increases the magnitude of the photocurrent at the junction and then reaches the maximum at V_G= -21.5 V. After this peak the photocurrent decreases and reaches the same photocurrent value of the substrate. The photothermoelectric response at the hBN and SiO_2-supported junction become almost zero at V_G= -34.5 V meaning that the difference between the Seebeck coefficient of the supported part by hBN and SiO_2 is too small to generate photocurrent. The hBN-supported region of MoS_2 can become a p-doped semiconductor at larger negative gate voltages. Changing the polarity of the major charge carrier from electrons to holes will change the Seebeck coefficient of hBN-supported MoS_2 from negative to positive. Changing the Seebeck coefficient from negative to positive will reverse the polarity of the photocurrent generated at the hBN-supported region (points A and B in Figure 3.23c).

As can be seen from Figure 3.23d, the photocurrent response behavior of the points near the indium junction is different from the junction made by hBN. By decreasing the gate voltage, the photocurrent near the contact decreases. The different gating response near the junction with metallic contact indicates that different photocurrent mechanisms are responsible for photocurrent generation near the metallic contacts and substrate-engineered junction.
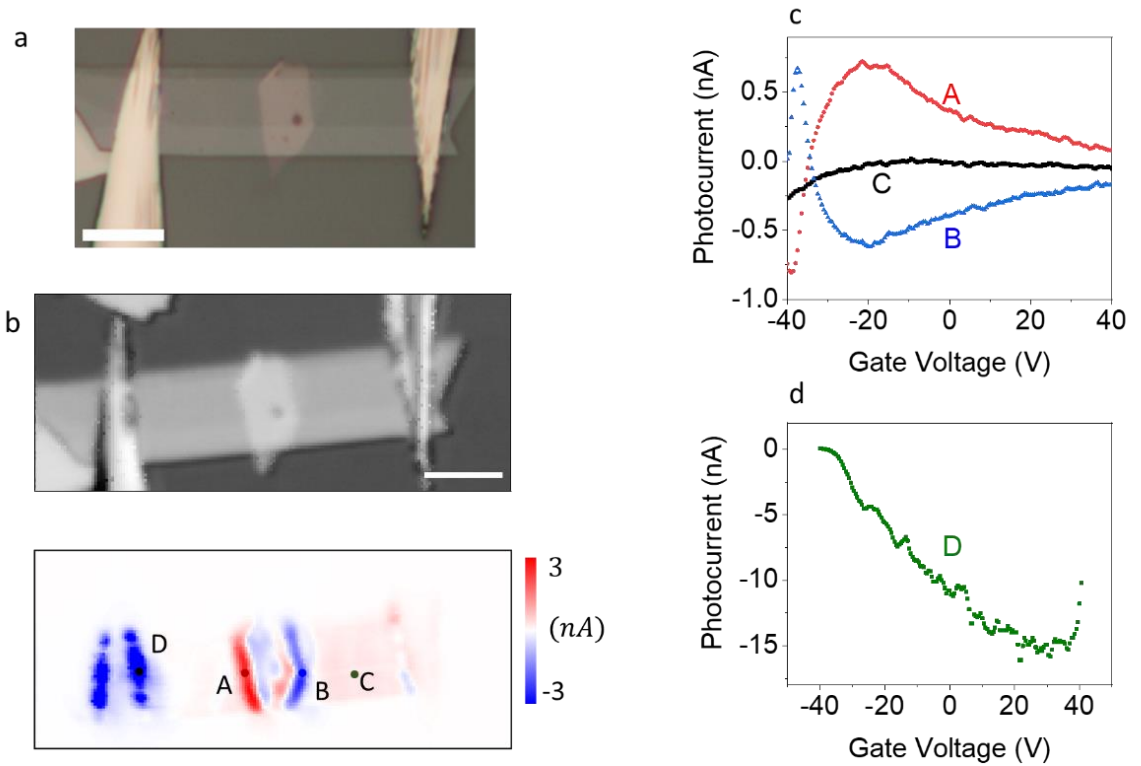
Figure 3.23 (a) Optical microscope image of the MoS_2 transferred on top of hBN flake. (b) The reflected intensity and SPCM maps using 85μW, 532 nm laser. The junction of SiO_2-supported and hBN-supported MoS_2 produces bipolar response. (c) and (d) Photocurrent data collected from points A, B, C and D. The photocurrent sign at points A and B changes at high negative gate voltage due to inversing the sign of the difference in Seebeck coefficient. Scale bars are 10 μm.

3.10   Conclusion

In summary, we fabricated a thermoelectric junction by engineering the substrate. The suspended region of the crystal exhibit redshift in Raman modes, indicating that the temperature rise due to the laser is higher than the supported region. The KPFM mapping of the suspended region showed different doping than the supported region, which can affect the Seebeck coefficient. The Seebeck coefficient difference between the supported and suspended parts forms a thermoelectric junction that generates photocurrent at zero bias. Finally, we showed that the difference in Seebeck can be modulated by gating.

Bibliography

[1]   M. Buscema, J.O. Island, D.J. Groenendijk, S.I. Blanter, G.A. Steele, H.S.J. van der Zant, A. Castellanos-Gomez, Photocurrent generation with two-dimensional van der Waals semiconductors, Chem. Soc. Rev. 44 (2015) 3691–3718. https://doi.org/10.1039/C5CS00106D.

[2]   T.S. Kasirga, D. Sun, J.H. Park, J.M. Coy, Z. Fei, X. Xu, D.H. Cobden, Photoresponse of a strongly correlated material determined by scanning photocurrent microscopy, Nat. Nanotechnol. 7 (2012) 723–727. https://doi.org/10.1038/nnano.2012.176.

[3]   O. Çakıroğlu, N. Mehmood, M.M. Çiçek, A. Aikebaier, H.R. Rasouli, E. Durgun, T.S. Kasırga, Thermal conductivity measurements in nanosheets via bolometric effect, 2D Mater. 7 (2020) 035003. https://doi.org/10.1088/2053-1583/ab8048.

[4]   X. Xu, N.M. Gabor, J.S. Alden, A.M. van der Zande, P.L. McEuen, Photo-Thermoelectric Effect at a Graphene Interface Junction, Nano Lett. 10 (2010) 562–566. https://doi.org/10.1021/nl903451y.

[5]   T.S. Kasirga, Thermal Conductivity Measurements in Atomically Thin Materials and Devices, Springer Singapore, Singapore, 2020. https://doi.org/10.1007/978-981-15-5348-6.

[6]   J.B. Herzog, M.W. Knight, D. Natelson, Thermoplasmonics: Quantifying plasmonic heating in single nanowires, Nano Lett. 14 (2014) 499–503. https://doi.org/10.1021/nl403510u.

[7]   H. Wei, D. Pan, S. Zhang, Z. Li, Q. Li, N. Liu, W. Wang, H. Xu, Plasmon Waveguiding in Nanowires, Chem. Rev. 118 (2018) 2882–2926. https://doi.org/10.1021/acs.chemrev.7b00441.

[8]   M. Song, A. Thete, J. Berthelot, Q. Fu, D. Zhang, G. Colas des Francs, E. Dujardin, A. Bouhelier, Electron-induced limitation of surface plasmon propagation in silver nanowires, Nanotechnology. 24 (2013) 095201. https://doi.org/10.1088/0957-4484/24/9/095201.

[9]   D. Langley, G. Giusti, C. Mayousse, C. Celle, D. Bellet, J.-P. Simonato, Flexible transparent conductive materials based on silver nanowire networks: a review, Nanotechnology. 24 (2013) 452001. https://doi.org/10.1088/0957-4484/24/45/452001.

[10]   C. Celle, C. Mayousse, E. Moreau, H. Basti, A. Carella, J.P. Simonato, Highly flexible transparent film heaters based on random networks of silver nanowires, Nano Res. 5 (2012) 427–433. https://doi.org/10.1007/s12274-012-0225-2.

[11]   P. Zolotavin, C.I. Evans, D. Natelson, Substantial local variation of the Seebeck coefficient in gold nanowires, Nanoscale. 9 (2017) 9160–9166. https://doi.org/10.1039/C7NR02678A.

[12]   C.I. Evans, R. Yang, L.T. Gan, M. Abbasi, X. Wang, R. Traylor, J.A. Fan, D. Natelson, Thermoelectric response from grain boundaries and lattice distortions in crystalline gold devices, Proc. Natl. Acad. Sci. 117 (2020) 23350–23355. https://doi.org/10.1073/pnas.2002284117.

[13]   P. Zolotavin, C. Evans, D. Natelson, Photothermoelectric Effects and Large Photovoltages in Plasmonic Au Nanowires with Nanogaps, J. Phys. Chem. Lett. 8 (2017) 1739–1744. https://doi.org/10.1021/acs.jpclett.7b00507.

[14]   M. Abbasi, C.I. Evans, L. Chen, D. Natelson, Single Metal Photodetectors Using Plasmonically-Active Asymmetric Gold Nanostructures, ACS Nano. 14 (2020) 17535–17542. https://doi.org/10.1021/acsnano.0c08035.

[15]   A. Harzheim, C. Evangeli, O. V. Kolosov, P. Gehring, Direct mapping of local Seebeck coefficient in 2D material nanostructures via scanning thermal gate microscopy, 2D Mater. 7 (2020) 1–19. https://doi.org/10.1088/2053-1583/aba333.

[16]   D.R. Ward, D.A. Corley, J.M. Tour, D. Natelson, Vibrational and electronic heating in nanoscale junctions, Nat. Nanotechnol. 6 (2011) 33–38. https://doi.org/10.1038/nnano.2010.240.

[17]   A. Stolz, J. Berthelot, M.M. Mennemanteuil, G. Colas Des Francs, L. Markey, V. Meunier, A. Bouhelier, Nonlinear photon-assisted tunneling transport in optical gap antennas, Nano Lett. 14 (2014) 2330–2338. https://doi.org/10.1021/nl404707t.

[18]   A.W. Sanders, D.A. Routenberg, B.J. Wiley, Y. Xia, E.R. Dufresne, M.A. Reed, Observation of Plasmon Propagation, Redirection, and Fan-Out in Silver Nanowires, Nano Lett. 6 (2006) 1822–1826. https://doi.org/10.1021/nl052471v.

[19]   A.L. Falk, F.H.L. Koppens, C.L. Yu, K. Kang, N. De Leon Snapp, A. V. Akimov, M.H. Jo, M.D. Lukin, H. Park, Near-field electrical detection of optical plasmons and single-plasmon sources, Nat. Phys. 5 (2009) 475–479. https://doi.org/10.1038/nphys1284.

[20] M. Razeghi, M. Üstünçelik, F. Shabani, H.V. Demir, T.S. Kasırga, Plasmon-enhanced photoresponse of single silver nanowires and their network devices, Nanoscale Horizons. 7 (2022) 396–402. https://doi.org/10.1039/d1nh00629k.

[21] H. Wei, F. Hao, Y. Huang, W. Wang, P. Nordlander, H. Xu, Polarization dependence of surface-enhanced Raman scattering in gold nanoparticle-nanowire systems, Nano Lett. 8 (2008) 2497–2502. https://doi.org/10.1021/nl8015297.

[22] S. Chang, H. Ko, R. Gunawidjaja, V. V. Tsukruk, Raman Markers from Silver Nanowire Crossbars, J. Phys. Chem. C. 115 (2011) 4387–4394. https://doi.org/10.1021/jp109348b.

[23] M.W. Knight, N.K. Grady, R. Bardhan, F. Hao, P. Nordlander, N.J. Halas, Nanoparticle-Mediated Coupling of Light into a Nanowire, Nano Lett. 7 (2007) 2346–2350. https://doi.org/10.1021/nl071001t.

[24] M.A. Mangold, C. Weiss, M. Calame, A.W. Holleitner, Surface plasmon enhanced photoconductance of gold nanoparticle arrays with incorporated alkane linkers, Appl. Phys. Lett. 94 (2009) 161104. https://doi.org/10.1063/1.3116148.

[25] A. V. Akimov, A. Mukherjee, C.L. Yu, D.E. Chang, A.S. Zibrov, P.R. Hemmer, H. Park, M.D. Lukin, Generation of single optical plasmons in metallic nanowires coupled to quantum dots, Nature. 450 (2007) 402–406. https://doi.org/10.1038/nature06230.

[26] O. Lopez-Sanchez, D. Lembke, M. Kayci, A. Radenovic, A. Kis, Ultrasensitive photodetectors based on monolayer MoS2, Nat. Nanotechnol. 8 (2013) 497–501. https://doi.org/10.1038/nnano.2013.100.

[27] S. Masubuchi, E. Watanabe, Y. Seo, S. Okazaki, T. Sasagawa, K. Watanabe, T. Taniguchi, T. Machida, Deep-learning-based image segmentation integrated with optical microscopy for automatically searching for two-dimensional materials, Npj 2D Mater. Appl. 4 (2020) 3. https://doi.org/10.1038/s41699-020-0137-z.

[28] B.-K. Kim, T.-H. Kim, D.-H. Choi, H. Kim, K. Watanabe, T. Taniguchi, H. Rho, J.-J. Kim, Y.-H. Kim, M.-H. Bae, Origins of genuine Ohmic van der Waals contact between indium and MoS2, Npj 2D Mater. Appl. 5 (2021) 9. https://doi.org/10.1038/s41699-020-00191-z.

[29] D. Lloyd, X. Liu, J.W. Christopher, L. Cantley, A. Wadehra, B.L. Kim, B.B. Goldberg, A.K. Swan, J.S. Bunch, Band Gap Engineering with Ultralarge Biaxial Strains in Suspended Monolayer MoS 2, Nano Lett. 16 (2016) 5836–5841. https://doi.org/10.1021/acs.nanolett.6b02615.

[30] L. Zhang, Z. Lu, Y. Song, L. Zhao, B. Bhatia, K.R. Bagnall, E.N. Wang, Thermal Expansion Coefficient of Monolayer Molybdenum Disulfide Using Micro-Raman Spectroscopy, Nano Lett. 19 (2019) 4745–4751.

https://doi.org/10.1021/acs.nanolett.9b01829.

[31] S. Sahoo, A.P.S. Gaur, M. Ahmadi, M.J.F. Guinel, R.S. Katiyar, Temperature-Dependent Raman Studies and Thermal Conductivity of Few-Layer MoS 2, J. Phys. Chem. C. 117 (2013) 9042–9047. https://doi.org/10.1021/jp402509w.

[32] J.J. Bae, H.Y. Jeong, G.H. Han, J. Kim, H. Kim, M.S. Kim, B.H. Moon, S.C. Lim, Y.H. Lee, Thickness-dependent in-plane thermal conductivity of suspended MoS 2 grown by chemical vapor deposition, Nanoscale. 9 (2017) 2541–2547. https://doi.org/10.1039/C6NR09484H.

[33] R. Yan, J.R. Simpson, S. Bertolazzi, J. Brivio, M. Watson, X. Wu, A. Kis, T. Luo, A.R. Hight Walker, H.G. Xing, Thermal Conductivity of Monolayer Molybdenum Disulfide Obtained from Temperature-Dependent Raman Spectroscopy, ACS Nano. 8 (2014) 986–993. https://doi.org/10.1021/nn405826k.

[34] O.E. Dagdeviren, O. Acikgoz, P. Grütter, M.Z. Baykara, Direct imaging, three-dimensional interaction spectroscopy, and friction anisotropy of atomic-scale ripples on MoS2, Npj 2D Mater. Appl. 4 (2020) 30. https://doi.org/10.1038/s41699-020-00164-2.

[35] J. Brivio, D.T.L. Alexander, A. Kis, Ripples and Layers in Ultrathin MoS2 Membranes, Nano Lett. 11 (2011) 5148–5153. https://doi.org/10.1021/nl2022288.

[36] S. Luo, G. Hao, Y. Fan, L. Kou, C. He, X. Qi, C. Tang, J. Li, K. Huang, J. Zhong, Formation of ripples in atomically thin MoS 2 and local strain engineering of electrostatic properties, Nanotechnology. 26 (2015) 105705. https://doi.org/10.1088/0957-4484/26/10/105705.

[37] W. Bao, F. Miao, Z. Chen, H. Zhang, W. Jang, C. Dames, C.N. Lau, Controlled ripple texturing of suspended graphene and ultrathin graphite membranes, Nat. Nanotechnol. 4 (2009) 562–566. https://doi.org/10.1038/nnano.2009.191.

[38] C. Lee, J. Hong, W.R. Lee, D.Y. Kim, J.H. Shim, Density functional theory investigation of the electronic structure and thermoelectric properties of layered MoS2, MoSe2 and their mixed-layer compound, J. Solid State Chem. 211 (2014) 113–119. https://doi.org/10.1016/j.jssc.2013.12.012.

[39] W. Wu, D. De, S.-C. Chang, Y. Wang, H. Peng, J. Bao, S.-S. Pei, High mobility and high on/off ratio field-effect transistors based on chemical vapor deposited single-crystal MoS 2 grains, Appl. Phys. Lett. 102 (2013) 142106. https://doi.org/10.1063/1.4801861.

[40] V. Mootheri, A. Leonhardt, D. Verreck, I. Asselberghs, C. Huyghebaert, S. de Gendt, I. Radu, D. Lin, M. Heyns, Understanding ambipolar transport in MoS 2 field effect transistors: the substrate is the key, Nanotechnology. 32

(2021) 135202. https://doi.org/10.1088/1361-6528/abd27a.

[41] H. Liu, K. Ba, S. Gou, Y. Kong, T. Ye, J. Ma, W. Bao, P. Zhou, D.W. Zhang, Z. Sun, Reversing the Polarity of MoS 2 with PTFE, ACS Appl. Mater. Interfaces. 13 (2021) 46117–46124. https://doi.org/10.1021/acsami.1c11328.

[42] D. Sun, G. Aivazian, A.M. Jones, J.S. Ross, W. Yao, D. Cobden, X. Xu, Ultrafast hot-carrier-dominated photocurrent in graphene, Nat. Nanotechnol. 7 (2012) 114–118. https://doi.org/10.1038/nnano.2011.243.

[43] M.M. Furchi, D.K. Polyushkin, A. Pospischil, T. Mueller, Mechanisms of Photoconductivity in Atomically Thin MoS 2, Nano Lett. 14 (2014) 6165– 6170. https://doi.org/10.1021/nl502339q.

[44] M. Buscema, M. Barkelid, V. Zwiller, H.S.J. van der Zant, G.A. Steele, A. Castellanos-Gomez, Large and Tunable Photothermoelectric Effect in Single-Layer MoS 2, Nano Lett. 13 (2013) 358–363. https://doi.org/10.1021/nl303321g.

[45] Y. Zhang, H. Li, L. Wang, H. Wang, X. Xie, S.-L. Zhang, R. Liu, Z.-J. Qiu, Photothermoelectric and photovoltaic effects both present in MoS2, Sci. Rep. 5 (2015) 7938. https://doi.org/10.1038/srep07938.

[46] W. Bao, X. Cai, D. Kim, K. Sridhara, M.S. Fuhrer, High mobility ambipolar MoS2 field-effect transistors: Substrate and dielectric effects, Appl. Phys. Lett. 102 (2013) 042104. https://doi.org/10.1063/1.4789365.

[47] H.K. Ng, D. Chi, K. Hippalgaonkar, Effect of dimensionality on thermoelectric powerfactor of molybdenum disulfide, J. Appl. Phys. 121 (2017) 204303. https://doi.org/10.1063/1.4984138.

[48] Y.-J. Kang, J. Kang, K.J. Chang, Electronic structure of graphene and doping effect on SiO2, Phys. Rev. B. 78 (2008) 115404. https://doi.org/10.1103/PhysRevB.78.115404.

[49] T. Jin, J. Kang, E. Su Kim, S. Lee, C. Lee, Suspended single-layer MoS2 devices, J. Appl. Phys. 114 (2013). https://doi.org/10.1063/1.4827477.

[50] F. Ye, Q. Liu, B. Xu, P.X.-L. Feng, X. Zhang, Very High Interfacial Thermal Conductance in Fully hBN-Encapsulated MoS2 van der Waals Heterostructure, (2021) 1–22. http://arxiv.org/abs/2102.05239.

[51] W. Wang, L. Zhou, S. Hu, K.S. Novoselov, Y. Cao, Visualizing Piezoelectricity on 2D Crystals Nanobubbles, Adv. Funct. Mater. 31 (2021) 2005053. https://doi.org/10.1002/adfm.202005053.